High-content high-resolution microscopy and deep learning assisted analysis reveals host and bacterial heterogeneity during *Shigella* infection.

Ana T. López-Jiménez*, Dominik Brokatzky, Kamla Pillay, Tyrese Williams, Gizem Özbaykal Güler and Serge Mostowy*.

* Corresponding authors: ana.lopezjimenez@lshtm.ac.uk, serge.mostowy@lshtm.ac.uk

Department of Infection Biology, London School of Hygiene and Tropical Medicine, Keppel Street, London WC1E 7HT, United Kingdom

Keywords: heterogeneity, high-content imaging, deep learning, septins, *Shigella*.

Abstract

Shigella flexneri is a Gram-negative bacterial pathogen and causative agent of bacillary dysentery. *S. flexneri* is closely related to *Escherichia coli* but harbors a virulence plasmid that encodes a Type III Secretion System (T3SS) required for host cell invasion. Widely recognized as a paradigm for research in cellular microbiology, *S. flexneri* has emerged as important to study mechanisms of cell-autonomous immunity, including septin cage entrapment. Here we use high-content high-resolution microscopy to monitor the dynamic and heterogeneous *S. flexneri* infection process by assessing multiple host and bacterial parameters (DNA replication, protein translation, T3SS activity). In the case of infected host cells, we report a reduction in DNA and protein synthesis together with morphological changes that suggest *S. flexneri* can induce cell-cycle arrest. We developed an artificial intelligence image analysis approach using Convolutional Neural Networks to reliably quantify, in an automated and unbiased manner, the recruitment of

SEPT7 to intracellular bacteria. We discover that heterogeneous SEPT7 assemblies are recuited to actively pathogenic bacteria with increased T3SS activation. Our automated microscopy workflow is useful to illuminate host and bacterial dynamics at the single-cell and population level, and to fully characterise the intracellular microenvironment controlling the *S. flexneri* infection process.

Introduction

Shigella flexneri is a Gram-negative bacterium and the etiologic agent of bacillary dysentery, an intestinal infectious disease that kills more than 150 thousand people worldwide per year, disproportionally affecting children under 5 years old from low- and middle-income countries (Global Burden of Disease Collaborative Network., 2020). After the ingestion of a small number of bacteria (10-100), *S. flexneri* rapidly colonises the human intestinal epithelium. For this, *S. flexneri* uses a Type 3 Secretion System (T3SS) that injects bacterial effectors into the host cell to modulate key aspects of the infection process and to evade innate immune defences by the host (Schnupf & Sansonetti, 2019). Following uptake by host cells, *S. flexneri* breaks its vacuolar compartment to access the cytosol (Ray et al., 2010). Here, the virulence factor IcsA enables *S. flexneri* to hijack host actin and polymerise comet tails that render bacteria motile to disseminate to neighbouring cells and spread in the tissue (Bernardini et al., 1989; Egile et al., 1999).

Septins are highly-conserved GTP-binding proteins that form heteromeric complexes (hexamers, octamers) that assemble into non-polar filaments, bundles and rings (Martins et al., 2023; Soroor et al., 2021; Szuba et al., 2021; Woods & Gladfelter, 2021). Septins are involved in many physiological cellular processes (eg. cytokinesis, cilia formation), and play key roles during infection (Mostowy & Cossart, 2012; Robertin & Mostowy, 2020; Spiliotis & Nakos, 2021). Septins form collar-like structures at the plasma membrane during bacterial invasion (Boddy et al., 2018; Mostowy et al., 2009; Robertin et al., 2023), and ring-like structures surrounding membrane protrusions in cell-to-cell bacterial spread (Mostowy et al., 2010). In the cytosol septins are recruited to actin-polymerising bacteria, including *S. flexneri* and *Mycobacterium marinum*, as cage-like structures (Mostowy et al., 2010). In the case of *S. flexneri*, septins are recruited to μm-scale curvature at bacterial poles and the division site, which are enriched in the negatively charged phospholipid cardiolipin (Krokowski et al., 2018). Recent work has shown that IcsA promotes the recruitment of septins to *S. flexneri*, and that lipopolysaccharide (LPS)

56 inhibits *S. flexneri*-septin cage entrapment (Lobato-Márquez et al., 2021; Mostowy et al., 2010).
57 Septin cages prevent bacterial actin tail motility and therefore are considered as an antibacterial
58 mechanism of host defence (Krokowski et al., 2018; Mostowy et al., 2010).
59 Intracellular infection is usually portrayed as a uniform, synchronised and highly orchestrated
60 process. However, infection assays performed in controlled laboratory environments with
61 isogenic populations display a high level of complexity (Avraham et al., 2015; Toniolo et al.,
62 2021). It is particularly unknown how different subsets of bacteria (eg. motile vs. non motile
63 bacteria) can colonise distinct intracellular microenvironments and become targeted by multiple
64 cell-autonomous immunity mechanisms (eg. septin cages, autophagy). It has been proposed that
65 this diversity of intracellular niches impacts bacterial physiology (Day et al., 2023; Gutierrez &
66 Enninga, 2022; Santucci et al., 2021). For example, it may affect individual bacterial ability to
67 acquire nutrients, to be exposed to varying antibiotic concentrations, or to elicit different
68 responses and signalling pathways within the host cell. While the concept of phenotypic
69 heterogeneity in prokaryotic clonal populations is well established (Ackermann, 2015), the
70 concept is emerging also in eukaryotic cells where non genetic differences may for instance
71 explain individual cell sensitivity and responses by cell-autonomous immunity (McDonald &
72 Dedhar, 2024). It is therefore paramount to study host and bacterial cells at the single-cell level,
73 to assess the individual responses that collectively contribute to the infection process.
74 Here, to dissect the complexity of *S. flexneri* infection in epithelial cells, we use high-content
75 high-resolution microscopy coupled to automated image analysis. High-content microscopy
76 enables the automated acquisition of thousands of microscopy images and therefore is useful to
77 capture the heterogeneity of individual host and bacterial cells during the infection process for
78 quantitative analysis (Aylan et al., 2023; Brodin & Christophe, 2011; Deboosere et al., 2021;
79 Dramé et al., 2023; Fisch et al., 2019a; Lensen et al., 2023; Pylkkö et al., 2021). We analyse
80 multiple parameters, such as morphological host cell features, the *de novo* synthesis of DNA and

81 proteins in both host and bacterial cells, as well as activation of the bacterial T3SS. To investigate
82 the antimicrobial potential of septin-mediated immunity, we develop a deep-learning based
83 approach to automatically identify septin-*S. flexneri* interactions. Together, we highlight the
84 power of high-content microscopy and artificial intelligence to reveal insights on both host and
85 bacterial cells, and illuminate fundamental biology underlying the *S. flexneri* infection process.

Results

Capturing the heterogeneity of *S. flexneri* infection using high-content microscopy.

To understand the complexity and reveal the heterogeneity of *S. flexneri* infection in human epithelial cells, we dissected the infection process using high-content high-resolution microscopy (**Figure 1A, B**). We observed a mean of 11.5% of infected cells measured by fluorescence at 3h 40 min post infection (hpi) at MOI 100:1 (**Figure 1C**). These infected cells presented different burdens of bacteria following an exponential decay distribution (**Figure 1D**), reflective of the formation of infection foci (Ortega et al., 2019). With growing evidence of the cytosol being a non-homogeneous compartment containing concentration gradients, biomolecular condensates, protein complexes and concentrates (van Tartwijk & Kaminski, 2022), we tested whether *S. flexneri* may be exposed to different intracellular microenvironments. For this, we measured the distance of bacteria to the centroid of cells (**Figure 1E**) and observed a median distance of 8.74 µm. The median distance to the centroid of the cell significantly decreased with increasing bacterial burden (**Figure 1E**), suggesting that the microenvironment of bacteria is diverse and changes as bacteria replicate intracellularly and populate the central parts of host cytosol after uptake at the host cell periphery. To dissect the heterogeneity in host cells, we quantified an increase of 36.9% and 22.3% in the cellular and nuclear area of infected cells, respectively (**Figure 1G, I**), which was dependent on the infection burden (**Figure 1H, J**). To test whether this increase reflected an increase in volume, we measured the total amount of Hoechst fluorescence in the nucleus of the cell as a proxy for nuclear volume (**Figure 1-figure supplement 1A**) and observed a 29.4% increase in infected cells. To test if this effect was due to morphological rearrangements during infection, we treated cells with Latrunculin B to inhibit actin polymerisation. While cells treated with Latrunculin B decreased their cellular area (but not their nuclear area) (**Figure 1-figure supplement 1B, C**), the drug did not abrogate the difference

110 in size between infected and uninfected cells. Taken together, these results highlight an increase
111 in cellular volume during infection that is dependent on the infection burden.
112
113 **Epithelial cells reduce *de novo* DNA and protein synthesis upon infection.**
114 In order to understand the physiological state of enlarged epithelial cells infected with *S. flexneri*,
115 we monitored host DNA replication and protein translation using Click-chemistry. Using a 1 h
116 pulse of the clickable thymidine analogue Edu, we specifically visualized and quantified *de novo*
117 DNA synthesis in the population of epithelial cells with high-content microscopy (**Figure 2A,**
118 **Figure 2-figure supplement 1**). We identified the subpopulation of cells in S-phase by their high
119 level of Edu incorporation. Consistent with this, this subpopulation of cells was fully abrogated
120 in the presence of the S-phase blocker Aphidicolin (Pedrali-Noy et al., 1980) (**Figure 2-figure**
121 **supplement 2A, B**). Approximately one third of uninfected cells (34.45%) were found in S-
122 phase (**Figure 2B, C**), in agreement with S-phase lasting around one third of the cell cycle (~8h
123 out of ~22h). Infected cells presented a similar proportion of cells in S-phase (35.89%), indicating
124 that *S. flexneri* infection did not block transition of cells from G1 to S at the timepoint tested. We
125 then assessed the amount of *de novo* DNA synthesis incorporated in cells in S-phase during
126 infection. Surprisingly, we observed a reduction of Edu incorporation in infected cells (**Figure**
127 **2D**), which was dependent on the bacterial burden (**Figure 2E**). These results indicate that *S.*
128 *flexneri* infection slows down DNA synthesis of epithelial cells.
129 To assess protein translation, we used a 1h pulse of the clickable methionine analogue AHA,
130 which specifically labels *de novo* synthesized proteins as AHA incorporation is reduced after
131 treatment with the inhibitor of translational elongation Cycloheximide (Ennis & Lubin, 1964)
132 (**Figure 2-figure supplement 1C, D**). During infection, we observed a reduction of protein
133 translation in infected cells compared to non-infected cells (**Figure 2F,G**), which was also
134 dependent on the bacterial burden (**Figure 2H**).

135 Collectively, the cell size increase together with the reduction of *de novo* DNA and protein
136 synthesis in infected epithelial cells suggests that *S. flexneri* induces an arrest in the host cell
137 cycle.
138
139 **Design of a deep learning pipeline to automatically identify bacteria interacting with**
140 **SEPT7.**
141 *S. flexneri* have been shown to interact with septins during infection. These interactions include
142 septin ring-like structures surrounding phagocytic cups, autophagosomes, actin tails and
143 protrusions, all being morphologically diverse structures that are normally scored by hand
144 (Krokowski et al., 2018; Lobato-Márquez et al., 2023; Mostowy et al., 2010) . To study septin-
145 associated bacteria using high-content microscopy, we designed a tailored analysis pipeline for
146 the automatic and unbiased identification of SEPT7-bacteria interactions (**Figure 3**). SEPT7 is a
147 core component of septin hexamers and octamers, and is historically used to identify septin
148 structures (Mostowy et al., 2010). The analysis pipeline includes two deep learning models based
149 on Convolutional Neural Networks (CNN), which are effective in solving classification tasks in
150 computer vision (Krizhevsky et al., n.d.; Lecun et al., 2015; Nielsen, 2015). As septins can
151 surround individual and also multiple bacteria simultaneously (**Figure 4-figure supplement**
152 **1A**), we focused on individual bacteria. For this, we trained the first classification model to
153 discriminate between "single" bacteria and "clumps". The second classification model was
154 designed to assign those single bacteria into "SEPT7-positive structures" or alternatively
155 "negatives", according to the morphology of SEPT7 recruitment around them.
156 The first classification model (discerning "single" versus "clumped" bacteria) together with its
157 training and performance metrics is summarized in **Figure 4**. A large dataset of annotated
158 bacteria (**Figure 4A, B, Figure 4-figure supplement 1B**) was used to train a Sequential model
159 with a typical CNN architecture that was experimentally tested and optimised accordingly for

160 best results (**Figure 4C**). This model provided a good fit of the training data (high accuracy, low
161 loss), with similar predictive power for the validation dataset (**Figure 4D, E**). Performance of the
162 model was further assessed with a confusion matrix where a separate annotated test dataset was
163 challenged and correct number of predictions scored, showing that 96% of SEPT7 structures and
164 83% of clumps were correctly identified (**Figure 4F**). Finally, effective performance of the model
165 was ensured with high values achieved in additional metrics testing for type I and II errors
166 (precision, recall, F1-score) (**Figure 4G**).
167 The second classification task (identification of "SEPT7 positive" vs "negative" bacteria) was
168 more challenging due to their intrinsic heterogeneity plus the presence of ubiquitious SEPT7
169 filaments that populate the vicinity of bacteria (but do not associate with bacteria per se). To
170 address these challenges, we increased the amount of data and complexity of the second
171 classification model (**Figure 4H-J, Figure 4-figure supplement 1C**) compared to the first
172 (**Figure 4A-C**). This included more than 1200 images of *S. flexneri* associated to SEPT7, both
173 from infections with wild-type bacteria or expressing AfaI to increase bacterial invasion. The
174 training process achieved a high accuracy and low loss for the training and validation dataset
175 (**Figure 4K, L**). Correct prediction of manually annotated SEPT7 positive structures was 80%
176 as shown in the confusion matrix (**Figure 4M**), with performance metrics Precision, Recall and
177 F1 score also around 0.8 (**Figure 4N**).
178
179 **Characterization of the morphological heterogeneity of SEPT7 recruitment to *S. flexneri*.**
180 The training of the classification model to identify bacteria associated to SEPT7 required a large
181 dataset of images. We observed diverse morphological conformations of SEPT7 signal around
182 bacteria (**Figure 5 A-C**). We differentiated five frequent subcategories from a total of 855 cases.
183 The first corresponds to most cases (66.7%), where SEPT7 forms rings that entrap bacteria
184 transversally (**Figure 5A, B, a**). We also observed two categories where SEPT7 surrounds

185 bacteria more homogeneously either in a tight (18.2%) or loose association (6.1%) (**Figure 5A,**
186 **B, b-c**). Finally, we observed partial SEPT7 recruitment, with only one (5.0%) or two (4.0%)
187 bacterial poles being targeted (**Figure 5A, B, d-e**). Given this diversity, we combined the entire
188 dataset to summarise the probability of SEPT7 interactions with bacteria (**Figure 5-figure**
189 **supplement 1**). As bacteria are found in any orientation inside epithelial cells, we included only
190 those instances where the z-projection of the bacterial axis measured more than 2.5µm, ensuring
191 they were positioned horizontally when imaged. Representations shown in **Figure 5-figure**
192 **supplement 1A, C** and graphs in **Figure 5-figure supplement 1B, D** can be understood as a
193 probability map of the area of influence of SEPT7 when associating with intracellular *S. flexneri*.
194

195 **SEPT7 is recruited to *S. flexneri* with increased T3SS activity.**

196 Septins have previously been shown to recognise growing bacterial cells *in vitro* and during
197 infection of HeLa cells, using pharmacologic and genetic manipulation (Krokowski et al., 2018;
198 Lobato-Márquez et al., 2021). To test the metabolic state of SEPT7-associated *S. flexneri* at 3h
199 40 min post infection (hpi) we used our high-content imaging and analysis pipeline (**Figure 6**).
200 We measured *S. flexneri de novo* synthesis of DNA and proteins using a 1 h pulse Click-IT Edu
201 and Click-IT AHA. Only active bacteria incorporated these analogues, as the antibiotic Nalidixic
202 acid (inhibitor of the bacterial DNA gyrase (Sugino et al., 1977)) and Rifampicin (inhibitor of
203 the bacterial RNA polymerase (Ezekiel & Hutchins, 1968)) significally reduced their
204 incorporation, respectively (**Figure 6-figure supplement 1A-D, Figure 6-figure supplement**
205 **1E,F)**. During infection, bacteria associated with SEPT7 showed heterogeneus levels of DNA
206 synthesis and protein translation similar to SEPT7-negative bacteria (**Figure 6A-H**).
207 *S. flexneri* pathogenicity relies on its T3SS. To understand effector secretion at the individual
208 bacterial level, we used *S. flexneri* expressing the Transcription-based Secretion Activity
209 Reporter (TSAR) (Campbell-Valois et al., 2014). This reporter comprises a short lived fast-

210 maturing superfolder GFP (GFPmsf2) that is expressed in conditions where the T3SS is active,
211 such as in broth upon addition of congo red (**Figure 7-figure supplement 1A, B**) (Parsot et al.,
212 1995) and during infection (**Figure 7**). We observed heterogeneity in TSAR signal (**Figure**
213 **9A,B**). T3SS activation was higher in bacteria found in cells with a low bacterial burden (less
214 than 10 intracellular bacteria) (**Figure 7A,C**). This suggests the highest level of activation occurs
215 in bacterial pioneers that colonise neighbouring cells, in agreement with (Campbell-Valois et al.,
216 2014). We then assessed T3SS activation in *S. flexneri* associated with SEPT7 using our deep
217 learning analysis pipeline (**Figure 7D-H**). We detected a significant increase in the percentage
218 of TSAR-positive *S. flexneri* and the overall intensity of TSAR signal compared to SEPT7-
219 negative bacteria (**Figure 7G,H**). These include SEPT7-associated protrussions and cage-like
220 structures (**Figure 7E**, **Figure 7-figure supplement 1C**). These data underscore the
221 antimicrobial role of septins in associating with actively pathogenic bacteria.
222

223 **Discussion**

224 Unravelling the intrinsic heterogeneity of host and bacterial cells underlying the infection process
225 is paramount to design effective therapeutic strategies. High-content and high-throughput image
226 analysis are ideal tools to capture this heterogeneity when coupled to automatic phenotypic image
227 analysis (Eliceiri et al., 2012; Mattiazzi Usaj et al., 2016; Pegoraro & Misteli, 2017). Here we
228 use high-content high-resolution microscopy and automated image analysis to quantitatively
229 dissect the heterogeneity of *S. flexneri* in epithelial cells at the single-cell and population level at
230 unprecedented subcellular detail.
231 We discover that *S. flexneri* induces important physiological changes in epithelial cells after
232 3h40min post infection. These include a marked decrease of DNA synthesis in cells in S-phase,
233 a collective shutdown of protein translation, and a larger cellular and nuclear area, all in a
234 bacterial-burden dependent manner. Collectively, these observations suggest *S. flexneri* infection

235 induces host cell stress and a halt in the normal progression of the cell cycle. Consistent with
236 this, *S. flexneri* has been shown to induce genotoxic stress (Bergounioux et al., 2012), inhibit
237 translation and induce formation of stress granules (Zhang et al., 2024), and block the G2/M
238 phase transition (Iwai et al., 2007; Wang et al., 2019). In the natural *S. flexneri* niche of the human
239 gut, such an arrest would prevent maturation and shedding of infected epithelial cells, thereby
240 promoting efficient gut colonisation (Iwai et al., 2007).
241 To understand how bacteria are targeted by cell-autonomus immune defences, such as septin
242 cage entrapment, it is necessary to investigate phenotypic characteristics of targeted bacteria and
243 the heterogeneous recruitment of cell-autonomous immune factors. While traditional image
244 segmentation tools fail to enable this task, rapidly evolving developments in the field of computer
245 vision are democratising the use of deep learning and CNNs for multiple applications (Berg et
246 al., 2019; Hung et al., 2020; Stringer et al., 2020; von Chamier et al., 2021; Weigert et al., 2020)
247 including infection biology (Davidson et al., 2021; Fisch et al., 2019b, 2021; Touquet et al.,
248 2018). However, the analysis of complex datasets still requires a tailored approach, as shown
249 here for bacterial interactions with the septin cytoskeleton (which is ubiquitious in the cell and
250 forms diverse assemblies whose precise identifcation requires high resolution). We successfully
251 implement a CNN based approach for the automated classification of bacteria associated with
252 SEPT7 assemblies, enabling the analysis of thousands of bacterial cells while saving time and
253 preventing human bias.
254 A large dataset of images depicting *S. flexneri* – SEPT7 interactions was acquired to train the
255 deep learning algorithm and to characterize the diversity of these structures. We observe that the
256 most frequent septin assembly is in the form of rings transversally surrounding the bacterial
257 surface. We also detected alternative morphologies, including homogeneous SEPT7 labelling
258 surrounding the bacterial surface (tight vs loose), as well as the discrete recruitment of SEPT7 to
259 one or two bacterial poles. While previous work has shown that septin cage assembly around *S.*

260 *flexneri* can start with the discrete recruitment of septins to one or two bacterial poles (Krokowski
261 et al., 2018), it is not yet known if the different septin assemblies we describe here correspond to
262 different stages or fates of the same structure or whether it marks separate biological events.
263 We use deep learning analysis to interrogate intracellular bacteria and show that *S. flexneri*
264 associated with SEPT7 present heterogenous DNA and protein synthesis. In addition, we show
265 that bacteria associated with SEPT7 have increased T3SS activity (as compared to bacteria not
266 associated with SEPT7) indicating that SEPT7 is recruited to actively pathogenic bacteria. T3SS
267 activity has been shown to be higher in motile bacteria (Campbell-Valois et al., 2014) which
268 reinforces the antimicrobial role of septins in counteracting actin tail motility. Altogether, our
269 deep learning tool to analyse septin-bacteria interactions opens the door to future studies on
270 interactions between bacteria and components of cell-autonomous immunity.
271

272 **Concluding remarks**

273 Heterogeneity in a controlled lab environment is only a small representation of the broader
274 heterogeneity underlying the clinical infection process, considering the genetic background of
275 the patient, interactions with microbiota, etc. In the future, our pipeline can be applied to
276 investigate septin-bacteria interactions among different *Shigella* spp. or clinically relevant
277 strains, as well as other intracellular bacteria (eg. *M. marinum, Staphylococcus aureus*,
278 *Pseudomonas aeruginosa*). In addition, our pipeline can be adapted to identify and score other
279 cytoskeletal structures (such as actin tails) or membrane organelles (such as autophagosomes)
280 associated with intracellular bacteria. Ultimately, we envision that our automated microscopy
281 workflows will help to screen pharmacologic or genetic libraries in a multiparametric manner
282 and understand their impact on host and bacterial cells at the single-cell and population level. In
283 this way, novel host and bacterial factors underlying heterogeneity and bacterial pathogenesis

284 could be identified, leading to transformative therapeutic strategies to combat bacterial infection

285 in humans.

286

287 **Materials and methods**

288 **Reagents.** The following antibodies were used: rabbit anti-SEPT7 (1:100 dilution, #18991, IBL),
289 Alexa-488-conjugated anti-rabbit antibody (1:500, #10729174, ThermoFisher Scientific), Alexa-
290 647-conjugated anti-rabbit antibody (1:500, #A27040, ThermoFisher Scientific). The following
291 dyes were used: Alexa-647-conjugated phalloidin (1:500, #10656353, ThermoFisher Scientific),
292 Hoechst (1:500, #H3570, ThermoFisher Scientific), 0.01% (w/v) congo red (#C6767, Sigma-
293 Aldrich). The following drugs were used: 50 µg/mL aphidicolin (#A0781 Sigma-Aldrich), 50
294 µg/mL cycloheximide (#2112 Cell Signalling), 2 µg/mL nalidixic acid (#N8878 Sigma-Aldrich),
295 and 100 µg/ml rifampicin (#R3501 Sigma-Aldrich).

296 **Bacterial strains and culture conditions.** The bacterial strains and plasmids described in this
297 study are listed in **Sup. Table 1**. *Shigella flexneri* 5a str. M90T mCherry was used throughout
298 the manuscript unless indicated otherwise unless indicated otherwise. *S. flexneri* strains were
299 grown in trypticase soy broth (TCS) agar containing congo red to select for red colonies,
300 indicative of a functional T3SS. Conical polypropylene tubes (#CLS430828, Corning) containing
301 5 ml of TCS were inoculated with individual red colonies of *S.flexneri* and were grown ~16 h at
302 37 °C with shaking at 200 rpm. The following day, bacterial cultures were diluted in fresh
303 prewarmed TCS (1:50 or 1:100 v/v), and cultured until an optical density (OD, measured at 600
304 nm) of 0.6.

305 **Cloning.** Primers used in this study were designed using NEBuilder Assembly Tool
306 (https://nebuilder.neb.com/#!/). To produce *S. flexneri* expressing AfaI and GFP, the pACAfaI
307 plasmid was constructed (plasmids characteristics and primer sequences are located in
308 **Supplementary Table 1**). Briefly, the *afaI* operon together with the amp^R gene was amplified
309 from *S.flexneri afaI* strain using the primers *afaI-operon-fw* and *afaI-operon-rv*. The *ori p15A*
310 was amplified from pAC-P_{lac} using the primers *p15A-ori-fw* and *p15A-ori-fw.* Both DNA
311 fragments were assembled using the Gibson assembly to generate the plasmid pAC-AfaI-AmpR.

312 In a second step, the *AmpR* gene from pAC-AfaI-Amp was substituted by the *CmR* gene and
313 generate pAC-AfaI-Cm. This was achieved by amplification of the *CmR* gene from pNeae2 using
314 the primers *CmR-fw CmR-rv* and amplification of the backbone of pAC-AfaI-Amp with primers
315 *afaI-p15A-fw, afaI-p15A-rv*, followed by Gibson assembly. Gibson assembly was performed at
316 50 °C for 30 min using the HiFi DNA Assembly Master Mix (#E2621L, New England Biolabs).
317 Resulting plasmid pAC-AfaI-Cm was transformed into *S. flexneri* GFP by electroporation.
318 **Mammalian cell culture.** HeLa (ATCC CCL-2) cells were grown at 37 °C and 5% CO_2 in
319 Dulbecco's modified Eagle medium (DMEM, GIBCO) supplemented with 10% fetal bovine
320 serum (FBS, Sigma-Aldrich).
321 **Infection of human cells.** Hela cells were seeded in 96-well microplates (PhenoPlates, Perkin
322 Elmer) at a confluency of 10^4 cells/well 2 days prior to infection. Alternatively, 9×10^4 HeLa
323 cells were seeded in 6-well plates (Thermo Scientific) containing 22 × 22 mm glass coverslips 2
324 days before the infection. Bacterial cultures were grown as described and cell cultures were
325 infected with *S. flexneri* strains as described previously (Mostowy et al., 2010). Briefly, Hela
326 cells were infected with *S. flexneri* by spin-inoculation at 110 g for 10 min at a multiplicity of
327 infection (MOI, bacteria:cell) of 100:1. Then, microplates were placed at 37 °C and 5% CO_2 for
328 30 min. Infected cultures were washed 3 × with phosphate-buffered saline (PBS) pH 7.4 and
329 incubated with fresh DMEM containing 10% FBS and 50 mg/mL gentamicin at 37 °C and 5%
330 CO_2 for 3 or 4 h. In order to obtain more instances of *S. flexneri* associated to SEPT7 in Figure
331 4H, one of the datasets was obtained after infection with *S. flexneri* expressing the adhesin AfaI
332 (Labigne-Roussel & Falkow, 1988) and GFP to increase host cell invasion at a MOI of 10 in the
333 absence of spin inoculation.
334 **Click chemistry.** To label *de novo* DNA and protein synthesis, Click-iT™ EdU Cell
335 Proliferation Kit for Imaging (#C10337 Thermofisher Scientific) and Click-iT™ AHA Protein
336 Synthesis HCS Assay (#C10289 Thermofisher Scientific) were used, respectively, according to

337 the manufacturer instructions. In the case of AHA, cells were cultured in glutamine, cystine and
338 methionine-free DMEM (#21013024 Thermofisher Scientific) for 1 h prior to the treatment.
339 10µM EdU and 25µM AHA were supplemented to live bacterial or mammalian cell cultures for
340 1h. Cells were fixed for immunofluorescence as indicated below. Click azide/alkyne reactions
341 were performed after permeabilization and prior to antibody staining as indicated below,
342 according to the manufacturer's instructions.

343 **Immunofluorescence and fluorescence microscopy.** Bacteria, coverslips or 96-well
344 microplates containing adherent infected or uninfected cells were washed three times with PBS
345 pH 7.4 and fixed 15 min in 4% paraformaldehyde (in PBS) at RT. Fixed cells were washed three
346 times with PBS pH 7.4 and subsequently permeabilized 5min with 0.1% Triton X-100 (in PBS).
347 Cells were then washed three times in PBS and incubated 1h with primary antibodies diluted in
348 PBS supplemented with 0.1% Triton X-100 and 1% bovine serum albumin. Cells were then
349 washed three times in PBS and incubated 45 min with anti-rabbit secondary antibodies diluted
350 0.1% Triton X-100 (in PBS), and Hoestch and Alexa-conjugated phalloidin where indicated. 96-
351 well microplates were washed three times in PBS and preserved in 0.01% sodium azide
352 (#10338380 Thermo Scientific) in PBS pH 7.4. Stained bacteria cultures and coverslips were
353 washed three times with PBS pH 7.4 mounted on glass slides with ProLong™ Diamond Antifade
354 Mountant (#P36970I Invitrogen). Fluorescence microscopy on stained bacteria was performed
355 using a using a 63×/1.4 C-Plan Apo oil immersion lens on a Zeiss LSM 880 confocal microscope
356 driven by ZEN Blacksoftware (v2.3). Microscopy images were obtained using z-stack image
357 series taking 8–16 slices. Fluorescence microscopy on infected or uninfected cells was performed
358 using a ZEISS Plan-APOCHROMAT 20× / 0.95 Autocorr Objective or a ZEISS Plan-
359 APOCHROMAT 50×/1.2 water immersion lens coupled to a 0.5x tubelens on a Zeiss
360 CellDiscoverer 7 with Airyscan detectors driven by ZEN Blue software (v3.5). Microscopy
361 images were obtained using z-stack image series taking 32 slices. Confocal images were

362 processed using Airyscan processing (Weinerfilter) using "Auto Filter" and "3D Processing"
363 options.

364 **Flow cytometry.** 5 x 10^4 individual bacterial cells were analysed using flow cytometry with an
365 LSRII flow cytometer (BD Biosciences). The data was analysed using FlowJo software, version
366 10.7.1. The median fluorescence of the bacterial population was determined and plotted for each
367 staining.

368 **Analysis pipelines.** Number of bacteria per cell, as well as fluorescence of bacteria, nuclei and
369 mammalian cells was analysed using Cellprofiler (v.4.0.7) (Carpenter et al., 2006). Custom made
370 segmentation and deep learning pipelines for the classification of septin cages were written in
371 ImageJ and Python using Keras.

372 **Statistics.** All graphs were plotted and statistical analysis were performed using Prism. n.s: non-
373 significant, *: p-value < 0.05, **: p-value < 0.01, ***: p-value < 0.001).

374 **Data availability**

375 Due to the size of the data, representative datasets were deposited in Dryad
376 (https://doi.org/10.5061/dryad.6wwpzgn5z). Materials and additional raw microscopy data can
377 be obtained from the corresponding authors upon requests.

378 **Code availability**

379 Custom ImageJ macros, phyton scripts and Jupyter notebooks were annotated and deposited in
380 Github (https://github.com/ATLopezJimenez/Toolset-high-content-analysis-of-Shigella-
381 infection).

382

383 **Acknowledgements**

384 We thank members of the Mostowy and Brian Ho labs for helpful discussion. We thank François-
385 Xavier Campbell-Valois for providing TSAR plasmids. We thank the instructors of the EMBL
386 course Deep Learning for Image Analysis, in particular Prof. Pejman Rasti. A.T.L.J. was funded

by the Swiss National Science Foundation Early Postdoc.Mobility Fellowship (P2GEP3_188277) and the European Union's Horizon 2020 research and innovation program under the Marie Skłodowska - Curie grant agreement no. H2020-MSCA-IF- 2020-895330. D.B. was supported by the Deutsche Forschungsgemeinschaft (DFG) Walter Benjamin Programme (BR 6637/1-1). G.Ö.G. is funded by the Human Frontier Science Program (LT000436/2021-L). Research in S. Mostowy laboratory is supported by a Wellcome Trust Senior Research Fellowship (206444/Z/17/Z) and European Research Council Consolidator Grant (772853 - ENTRAPMENT).

395 **Supplementary table S1.**

Bacterial strain	**Genotype**	**Reference**
Shigella flexneri srv. 5a str. M90T	SmR	(Mostowy et al., 2010)
S. flexneri mCherry	Constitutively producing mCherry, $Carb^R$, Sm^R	(Mostowy et al., 2013)
S. flexneri afaI	Constitutively producing the adhesin AfaE, Amp^R, Sm^R	(Mostowy et al., 2010)
S. flexneri GFP	Constitutively producing GFP, $Carb^R$	(Mostowy et al., 2010)
S. flexneri GFP *afaI*	Constitutively producing the adhesin AfaE and GFP, Amp^R Cm^R, Sm^R	This study
Plasmid	**Characteristics**	**Reference**
pTSAR1ud2.4s	T3SS reporter	(Campbell-Valois et al., 2014)
pAC-P_{lac}	pACYC184 derived plasmid.	(Lobato-Márquez et al., 2015)
pAC-AfaI-AmpR	For constitutive expression of the adhesin AfaE, ori p15A, Amp^R	This study
pAC-AfaI-CmR	For constitutive expression of the adhesin AfaE, ori p15A, Cm^R	This study
Primer	**Sequence (5'-3')**	**Reference**
afaI-operon-fw	tgcgttgcgcgaagatcctttgatcttttctacgggg	This study
afaI-operon-rv	ggaagctaaacgagcccgatcttcccca	This study
p15A-ori-fw	atcgggctcgtttagcttccttagctcc	This study
p15A-ori-rv	aaggatcttcgcgcaacgcaattaatgtaag	This study
afaI-p15A-fw	cggggcgtaactgtcagaccaagtttac	This study
afaI-p15A-rv	ttttctccatactcttccttttcaatattattg	This study
CmR-fw	aaggaagagtatggagaaaaaaatcactggatataccaccgttgatatatccc	This study
CmR-rv	ggtctgacagttacgccccgccctgcca	This study

396

397 **References**

398 Ackermann, M. (2015). A functional perspective on phenotypic heterogeneity in
399 microorganisms. *Nature Publishing Group*, *13*. https://doi.org/10.1038/nrmicro3491
400 Avraham, R., Haseley, N., Brown, D., Penaranda, C., Jijon, H. B., Trombetta, J. J., Satija, R.,
401 Shalek, A. K., Xavier, R. J., Regev, A., & Hung, D. T. (2015). Pathogen Cell-to-Cell
402 Variability Drives Heterogeneity in Host Immune Responses. *Cell*, *162*(6), 1309–1321.
403 https://doi.org/10.1016/J.CELL.2015.08.027
404 Aylan, B., Botella, L., Gutierrez, M. G., & Santucci, P. (2023). High content quantitative imaging
405 of Mycobacterium tuberculosis responses to acidic microenvironments within human
406 macrophages. *FEBS Open Bio*, *13*(7), 1204–1217. https://doi.org/10.1002/2211-
407 5463.13537
408 Berg, S., Kutra, D., Kroeger, T., Straehle, C. N., Kausler, B. X., Haubold, C., Schiegg, M., Ales,
409 J., Beier, T., Rudy, M., Eren, K., Cervantes, J. I., Xu, B., Beuttenmueller, F., Wolny, A.,
410 Zhang, C., Koethe, U., Hamprecht, F. A., & Kreshuk, A. (2019). ilastik: interactive machine
411 learning for (bio)image analysis. *Nature Methods 2019 16:12*, *16*(12), 1226–1232.
412 https://doi.org/10.1038/s41592-019-0582-9
413 Bergounioux, J., Elisee, R., Prunier, A. L., Donnadieu, F., Sperandio, B., Sansonetti, P., &
414 Arbibe, L. (2012). Calpain Activation by the Shigella flexneri Effector VirA Regulates Key
415 Steps in the Formation and Life of the Bacterium's Epithelial Niche. *Cell Host & Microbe*,
416 *11*(3), 240–252. https://doi.org/10.1016/J.CHOM.2012.01.013
417 Bernardini, M. L., Mounier, J., D'Hauteville, H., Coquis-Rondon, M., & Sansonetti, P. J. (1989).
418 Identification of icsA, a plasmid locus of Shigella flexneri that governs bacterial intra- and
419 intercellular spread through interaction with F-actin. *Proceedings of the National Academy*
420 *of Sciences of the United States of America*, *86*(10), 3867–3871.
421 https://doi.org/10.1073/PNAS.86.10.3867

422 Boddy, K. C., Gao, A. D., Truong, D., Kim, M. S., Froese, C. D., Trimble, W. S., & Brumell, J.
423 H. (2018). Septin-regulated actin dynamics promote Salmonella invasion of host cells.
424 *Cellular Microbiology*, *20*(10), e12866. https://doi.org/10.1111/CMI.12866
425 Brodin, P., & Christophe, T. (2011). High-content screening in infectious diseases. *Current*
426 *Opinion in Chemical Biology*, *15*(4), 534–539.
427 https://doi.org/10.1016/J.CBPA.2011.05.023
428 Campbell-Valois, F. X., Schnupf, P., Nigro, G., Sachse, M., Sansonetti, P. J., & Parsot, C. (2014).
429 A Fluorescent Reporter Reveals On/Off Regulation of the Shigella Type III Secretion
430 Apparatus during Entry and Cell-to-Cell Spread. *Cell Host & Microbe*, *15*(2), 177–189.
431 https://doi.org/10.1016/J.CHOM.2014.01.005
432 Carpenter, A. E., Jones, T. R., Lamprecht, M. R., Clarke, C., Kang, I. H., Friman, O., Guertin,
433 D. A., Chang, J. H., Lindquist, R. A., Moffat, J., Golland, P., & Sabatini, D. M. (2006).
434 CellProfiler: Image analysis software for identifying and quantifying cell phenotypes.
435 *Genome Biology*, *7*(10), 1–11. https://doi.org/10.1186/GB-2006-7-10-R100/FIGURES/4
436 Davidson, M. S., Andradi-Brown, C., Yahiya, S., Chmielewski, J., O'Donnell, A. J., Gurung, P.,
437 Jeninga, M. D., Prommana, P., Andrew, D. W., Petter, M., Uthaipibull, C., Boyle, M. J.,
438 Ashdown, G. W., Dvorin, J. D., Reece, S. E., Wilson, D. W., Cunningham, K. A., Ando, D.
439 Michael., Dimon, M., & Baum, J. (2021). Automated detection and staging of malaria
440 parasites from cytological smears using convolutional neural networks. *Biological Imaging*,
441 *1*, 2. https://doi.org/10.1017/S2633903X21000015
442 Day, N. J., Santucci, P., & Gutierrez, M. G. (2023). Host cell environments and antibiotic efficacy
443 in tuberculosis. *Trends in Microbiology*. https://doi.org/10.1016/J.TIM.2023.08.009
444 Deboosere, N., Belhaouane, I., Machelart, A., Hoffmann, E., Vandeputte, A., & Brodin, P.
445 (2021). High-Content Analysis Monitoring Intracellular Trafficking and Replication of

446 Mycobacterium tuberculosis Inside Host Cells. *Methods in Molecular Biology*, *2314*, 649–
447 702. https://doi.org/10.1007/978-1-0716-1460-0_29/COVER
448 Dramé, M., Garcia-Rodriguez, F. J., Buchrieser, C., & Escoll, P. (2023). High-content assay to
449 measure mitochondrial function and bacterial vacuole size in infected human primary
450 macrophages. *STAR Protocols*, *4*(2), 102175. https://doi.org/10.1016/J.XPRO.2023.102175
451 Egile, C., Loisel, T. P., Laurent, V., Li, R., Pantaloni, D., Sansonetti, P. J., & Carlier, M. F.
452 (1999). Activation of the Cdc42 Effector N-Wasp by the Shigella flexneri Icsa Protein
453 Promotes Actin Nucleation by Arp2/3 Complex and Bacterial Actin-Based Motility.
454 *Journal of Cell Biology*, *146*(6), 1319–1332. https://doi.org/10.1083/JCB.146.6.1319
455 Eliceiri, K. W., Berthold, M. R., Goldberg, I. G., Ibáñez, L., Manjunath, B. S., Martone, M. E.,
456 Murphy, R. F., Peng, H., Plant, A. L., Roysam, B., Stuurmann, N., Swedlow, J. R.,
457 Tomancak, P., & Carpenter, A. E. (2012). Biological imaging software tools. *Nature*
458 *Methods 2012 9:7*, *9*(7), 697–710. https://doi.org/10.1038/nmeth.2084
459 Ennis, H. L., & Lubin, M. (1964). Cycloheximide: Aspects of inhibition of protein synthesis in
460 mammalian cells. *Science*, *146*(3650), 1474–1476.
461 https://doi.org/10.1126/SCIENCE.146.3650.1474
462 Ezekiel, D. H., & Hutchins, J. E. (1968). Mutations affecting RNA Polymerase associated with
463 Rifampicin Resistance in Escherichia coli. *Nature 1968 220:5164*, *220*(5164), 276–277.
464 https://doi.org/10.1038/220276a0
465 Fisch, D., Evans, R., Clough, B., Byrne, S. K., Channell, W. M., Dockterman, J., & Frickel, E.
466 M. (2021). HRMAn 2.0: Next-generation artificial intelligence–driven analysis for broad
467 host–pathogen interactions. *Cellular Microbiology*, *23*(7), e13349.
468 https://doi.org/10.1111/CMI.13349

469 Fisch, D., Yakimovich, A., Clough, B., Wright, J., Bunyan, M., Howell, M., Mercer, J., &
470 Frickel, E. (2019a). Defining host–pathogen interactions employing an artificial intelligence
471 workflow. *ELife*, *8*. https://doi.org/10.7554/ELIFE.40560
472 Fisch, D., Yakimovich, A., Clough, B., Wright, J., Bunyan, M., Howell, M., Mercer, J., &
473 Frickel, E. (2019b). Defining host–pathogen interactions employing an artificial intelligence
474 workflow. *ELife*, *8*. https://doi.org/10.7554/ELIFE.40560
475 Global Burden of Disease Collaborative Network. (2020). *Global Burden of Disease Study 2019*
476 *(GBD 2019)*. Institute for Health Metrics and Evaluation (IHME).
477 Gutierrez, M. G., & Enninga, J. (2022). Intracellular niche switching as host subversion strategy
478 of bacterial pathogens. *Current Opinion in Cell Biology*, *76*, 102081.
479 https://doi.org/10.1016/J.CEB.2022.102081
480 Hung, J., Goodman, A., Ravel, D., Lopes, S. C. P., Rangel, G. W., Nery, O. A., Malleret, B.,
481 Nosten, F., Lacerda, M. V. G., Ferreira, M. U., Rénia, L., Duraisingh, M. T., Costa, F. T.
482 M., Marti, M., & Carpenter, A. E. (2020). Keras R-CNN: Library for cell detection in
483 biological images using deep neural networks. *BMC Bioinformatics*, *21*(1), 1–7.
484 https://doi.org/10.1186/S12859-020-03635-X/FIGURES/1
485 Iwai, H., Kim, M., Yoshikawa, Y., Ashida, H., Ogawa, M., Fujita, Y., Muller, D., Kirikae, T.,
486 Jackson, P. K., Kotani, S., & Sasakawa, C. (2007). A Bacterial Effector Targets Mad2L2,
487 an APC Inhibitor, to Modulate Host Cell Cycling. *Cell*, *130*(4), 611–623.
488 https://doi.org/10.1016/J.CELL.2007.06.043
489 Krizhevsky, A., Sutskever, I., & Hinton, G. E. (n.d.). *ImageNet Classification with Deep*
490 *Convolutional Neural Networks*. Retrieved 13 February 2024, from
491 http://code.google.com/p/cuda-convnet/
492 Krokowski, S., Lobato-Márquez, D., Chastanet, A., Pereira, P. M., Angelis, D., Galea, D.,
493 Larrouy-Maumus, G., Henriques, R., Spiliotis, E. T., Carballido-López, R., & Mostowy, S.

(2018). Septins Recognize and Entrap Dividing Bacterial Cells for Delivery to Lysosomes. *Cell Host & Microbe*, *24*(6), 866-874.e4. https://doi.org/10.1016/j.chom.2018.11.005

Labigne-Roussel, A., & Falkow, S. (1988). Distribution and degree of heterogeneity of the afimbrial-adhesin-encoding operon (afa) among uropathogenic Escherichia coli isolates. *Infection and Immunity*, *56*(3), 640–648. https://doi.org/10.1128/iai.56.3.640-648.1988

Lecun, Y., Bengio, Y., & Hinton, G. (2015). Deep learning. *Nature 2015 521:7553*, *521*(7553), 436–444. https://doi.org/10.1038/nature14539

Lensen, A., Gomes, M. C., López-Jiménez, A. T., & Mostowy, S. (2023). An automated microscopy workflow to study Shigella–neutrophil interactions and antibiotic efficacy in vivo. *DMM Disease Models and Mechanisms*, *16*(6). https://doi.org/10.1242/DMM.049908/307310/AM/AN-AUTOMATED-MICROSCOPY-WORKFLOW-TO-STUDY-SHIGELLA

Lobato-Márquez, D., Conesa, J. J., López-Jiménez, A. T., Divine, M. E., Pruneda, J. N., & Mostowy, S. (2023). Septins and K63 ubiquitin chains are present in separate bacterial microdomains during autophagy of entrapped Shigella. *Journal of Cell Science*, *136*(7). https://doi.org/10.1242/JCS.261139/VIDEO-6

Lobato-Márquez, D., Moreno-Córdoba, I., Figueroa, V., Diáz-Orejas, R., & Garciá-Del Portillo, F. (2015). Distinct type I and type II toxin-antitoxin modules control Salmonella lifestyle inside eukaryotic cells. *Scientific Reports 2015 5:1*, *5*(1), 1–10. https://doi.org/10.1038/srep09374

Lobato-Márquez, D., Xu, J., Güler, G. Ö., Ojiakor, A., Pilhofer, M., & Mostowy, S. (2021). Mechanistic insight into bacterial entrapment by septin cage reconstitution. *Nature Communications 2021 12:1*, *12*(1), 1–14. https://doi.org/10.1038/s41467-021-24721-5

Martins, C. S., Taveneau, C., Castro-Linares, G., Baibakov, M., Buzhinsky, N., Eroles, M., Milanović, V., Omi, S., Pedelacq, J.-D., Iv, F., Bouillard, L., Llewellyn, A., Gomes, M.,

519 Belhabib, M., Kuzmić, M., Verdier-Pinard, P., Lee, S., Badache, A., Kumar, S., …
520 Mavrakis, M. (2023). Human septins organize as octamer-based filaments and mediate
521 actin-membrane anchoring in cells. *Journal of Cell Biology*, *222*(3).
522 https://doi.org/10.1083/JCB.202203016/213778
523 Mattiazzi Usaj, M., Styles, E. B., Verster, A. J., Friesen, H., Boone, C., & Andrews, B. J. (2016).
524 High-Content Screening for Quantitative Cell Biology. *Trends in Cell Biology*, *26*(8), 598–
525 611. https://doi.org/10.1016/J.TCB.2016.03.008
526 McDonald, P. C., & Dedhar, S. (2024). Persister cell plasticity in tumour drug resistance.
527 *Seminars in Cell & Developmental Biology*, *156*, 1–10.
528 https://doi.org/10.1016/J.SEMCDB.2023.11.003
529 Mostowy, S., Bonazzi, M., Hamon, M. A., Tham, T. N., Mallet, A., Lelek, M., Gouin, E.,
530 Demangel, C., Brosch, R., Zimmer, C., Sartori, A., Kinoshita, M., Lecuit, M., & Cossart, P.
531 (2010). Entrapment of Intracytosolic Bacteria by Septin Cage-like Structures. *Cell Host &*
532 *Microbe*, *8*(5), 433–444. https://doi.org/10.1016/J.CHOM.2010.10.009
533 Mostowy, S., Boucontet, L., Mazon Moya, M. J., Sirianni, A., Boudinot, P., Hollinshead, M.,
534 Cossart, P., Herbomel, P., Levraud, J.-P. P., & Colucci-Guyon, E. (2013). The Zebrafish as
535 a New Model for the In Vivo Study of Shigella flexneri Interaction with Phagocytes and
536 Bacterial Autophagy. *PLoS Pathogens*, *9*(9), e1003588.
537 https://doi.org/10.1371/journal.ppat.1003588
538 Mostowy, S., & Cossart, P. (2012). Septins: the fourth component of the cytoskeleton. *Nature*
539 *Reviews Molecular Cell Biology*, *13*(3), 183–194. https://doi.org/10.1038/nrm3284
540 Mostowy, S., Nam Tham, T., Danckaert, A., Guadagnini, S., Boisson-Dupuis, S., Pizarro-Cerdá,
541 J., & Cossart, P. (2009). Septins Regulate Bacterial Entry into Host Cells. *PLoS ONE*, *4*(1),
542 e4196. https://doi.org/10.1371/journal.pone.0004196

543 Nielsen, M. A. (2015). *Neural Networks and Deep Learning*. Determination press.
544 http://neuralnetworksanddeeplearning.com
545 Ortega, F. E., Koslover, E. F., & Theriot, J. A. (2019). Listeria monocytogenes cell-to-cell spread
546 in epithelia is heterogeneous and dominated by rare pioneer bacteria. *ELife*, *8*.
547 https://doi.org/10.7554/ELIFE.40032
548 Parsot, C., Ménard, R., Gounon, P., & Sansonetti, P. J. (1995). Enhanced secretion through the
549 Shigella flexneri Mxi-Spa translocon leads to assembly of extracellular proteins into
550 macromolecular structures. *Molecular Microbiology*, *16*(2), 291–300.
551 https://doi.org/10.1111/J.1365-2958.1995.TB02301.X
552 Pedrali-Noy, G., Spadari, S., Miller-Faurès, A., Miller, A. O. A., Kruppa, J., & Koch, G. (1980).
553 Synchronization of HeLa cell cultures by inhibition of DNA polymerase alpha with
554 aphidicolin. *Nucleic Acids Research*, *8*(2), 377. https://doi.org/10.1093/NAR/8.2.377
555 Pegoraro, G., & Misteli, T. (2017). High-Throughput Imaging for the Discovery of Cellular
556 Mechanisms of Disease. *Trends in Genetics*, *33*(9), 604–615.
557 https://doi.org/10.1016/J.TIG.2017.06.005
558 Pylkkö, T., Ilina, P., & Tammela, P. (2021). Development and validation of a high-content
559 screening assay for inhibitors of enteropathogenic E. coli adhesion. *Journal of*
560 *Microbiological Methods*, *184*, 106201. https://doi.org/10.1016/J.MIMET.2021.106201
561 Ray, K., Bobard, A., Danckaert, A., Paz-Haftel, I., Clair, C., Ehsani, S., Tang, C., Sansonetti, P.,
562 Van Nhieu, G. T., & Enninga, J. (2010). Tracking the dynamic interplay between bacterial
563 and host factors during pathogen-induced vacuole rupture in real time. *Cellular*
564 *Microbiology*, *12*(4), 545–556. https://doi.org/10.1111/J.1462-5822.2010.01428.X
565 Robertin, S., Brokatzky, D., Lobato-Márquez, D., & Mostowy, S. (2023). Regulation of integrin
566 α5β1-mediated Staphylococcus aureus cellular invasion by the septin cytoskeleton.

European Journal of Cell Biology, *102*(4), 151359. https://doi.org/10.1016/J.EJCB.2023.151359

Robertin, S., & Mostowy, S. (2020). The history of septin biology and bacterial infection. *Cellular Microbiology*, *22*(4), e13173. https://doi.org/10.1111/CMI.13173

Santucci, P., Greenwood, D. J., Fearns, A., Chen, K., Jiang, H., & Gutierrez, M. G. (2021). Intracellular localisation of Mycobacterium tuberculosis affects efficacy of the antibiotic pyrazinamide. *Nature Communications 2021 12:1*, *12*(1), 1–15. https://doi.org/10.1038/s41467-021-24127-3

Schnupf, P., & Sansonetti, P. J. (2019). Shigella Pathogenesis: New Insights through Advanced Methodologies. In *Bacteria and Intracellularity* (pp. 15–39). American Society of Microbiology. https://doi.org/10.1128/microbiolspec.bai-0023-2019

Soroor, F., Kim, M. S., Palander, O., Balachandran, Y., Collins, R. F., Benlekbir, S., Rubinstein, J. L., & Trimble, W. S. (2021). Revised subunit order of mammalian septin complexes explains their in vitro polymerization properties. *Molecular Biology of the Cell*, *32*(3), 289–300. https://doi.org/10.1091/MBC.E20-06-0398/ASSET/IMAGES/LARGE/MBC-32-289-G004.JPEG

Spiliotis, E. T., & Nakos, K. (2021). Cellular functions of actin- and microtubule-associated septins. *Current Biology*, *31*(10), R651–R666. https://doi.org/10.1016/J.CUB.2021.03.064

Stringer, C., Wang, T., Michaelos, M., & Pachitariu, M. (2020). Cellpose: a generalist algorithm for cellular segmentation. *Nature Methods 2020 18:1*, *18*(1), 100–106. https://doi.org/10.1038/s41592-020-01018-x

Sugino, A., Peebles, C. L., Kreuzer, K. N., & Cozzarelli, N. R. (1977). Mechanism of action of nalidixic acid: Purification of Escherichia coli nalA gene product and its relationship to DNA gyrase and a novel nicking-closing enzyme. *Proceedings of the National Academy of Sciences*, *74*(11), 4767–4771. https://doi.org/10.1073/PNAS.74.11.4767

592 Szuba, A., Bano, F., Castro-Linares, G., Iv, F., Mavrakis, M., Richter, R. P., Bertin, A., &
593 Koenderink, G. H. (2021). Membrane binding controls ordered self-assembly of animal
594 septins. *ELife*, *10*. https://doi.org/10.7554/ELIFE.63349
595 Toniolo, C., Rutschmann, O., & McKinney, J. D. (2021). Do chance encounters between
596 heterogeneous cells shape the outcome of tuberculosis infections? *Current Opinion in*
597 *Microbiology*, *59*, 72–78. https://doi.org/10.1016/J.MIB.2020.08.008
598 Touquet, B., Pelissier, L., Cavailles, P., Yi, W., Bellini, V., Mercier, C., Cesbron-Delauw, M. F.,
599 Boumendjel, A., & Aldebert, D. (2018). High-content imaging assay to evaluate
600 Toxoplasma gondii infection and proliferation: A multiparametric assay to screen new
601 compounds. *PLOS ONE*, *13*(8), e0201678.
602 https://doi.org/10.1371/JOURNAL.PONE.0201678
603 van Tartwijk, F. W., & Kaminski, C. F. (2022). Protein Condensation, Cellular Organization, and
604 Spatiotemporal Regulation of Cytoplasmic Properties. *Advanced Biology*, *6*(11), 2101328.
605 https://doi.org/10.1002/ADBI.202101328
606 von Chamier, L., Laine, R. F., Jukkala, J., Spahn, C., Krentzel, D., Nehme, E., Lerche, M.,
607 Hernández-Pérez, S., Mattila, P. K., Karinou, E., Holden, S., Solak, A. C., Krull, A.,
608 Buchholz, T. O., Jones, M. L., Royer, L. A., Leterrier, C., Shechtman, Y., Jug, F., …
609 Henriques, R. (2021). Democratising deep learning for microscopy with ZeroCostDL4Mic.
610 *Nature Communications 2021 12:1*, *12*(1), 1–18. https://doi.org/10.1038/s41467-021-
611 22518-0
612 Wang, X., Pernicone, N., Pertz, L., Hua, D., Zhang, T., Listovsky, T., & Xie, W. (2019). REV7
613 has a dynamic adaptor region to accommodate small GTPase RAN/Shigella IpaB ligands,
614 and its activity is regulated by the RanGTP/GDP switch. *Journal of Biological Chemistry*,
615 *294*(43), 15733–15742. https://doi.org/10.1074/JBC.RA119.010123

Weigert, M., Schmidt, U., Haase, R., Sugawara, K., & Myers, G. (2020, March). Star-convex Polyhedra for 3D Object Detection and Segmentation in Microscopy. *2020 IEEE Winter Conference on Applications of Computer Vision (WACV)*. https://doi.org/10.1109/WACV45572.2020.9093435

Woods, B. L., & Gladfelter, A. S. (2021). The state of the septin cytoskeleton from assembly to function. *Current Opinion in Cell Biology*, *68*, 105–112. https://doi.org/10.1016/J.CEB.2020.10.007

Zhang, Q., Xian, W., Li, Z., Lu, Q., Chen, X., Ge, J., Tang, Z., Liu, B., Chen, Z., Gao, X., Hottiger, M. O., Zhang, P., Qiu, J., Shao, F., & Liu, X. (2024). Shigella induces stress granule formation by ADP-riboxanation of the eIF3 complex. *Cell Reports*, *43*(2), 113789. https://doi.org/10.1016/J.CELREP.2024.113789

629 **Figure legends.**

630 **Figure 1. High-content imaging captures the heterogeneity of *S. flexneri* infection.** (A)
631 Representative high-resolution microscopy image of HeLa cells infected with *S. flexneri*
632 expressing mCherry acquired with the high-content microscope ZEISS CellDiscoverer7. Scale
633 bar, 10 µm. (B) Enlarged view of insets in A, highlighting a *S. flexneri* bacteria polymerising an
634 actin tail (1) and entrapped in a septin cage (2), scale bar, 1 µm. (C) Percentage of infected cells
635 at 3 h.p.i. of 7 independent experiments. Graph represents mean = 11.49% ± SD = 4.36%. (D)
636 Percentage of infected cells harbouring different bacterial doses, graph represents mean ± SD.
637 (E) Distance of the bacteria to the centroid of the host cell. Graph represents the median (8.74
638 µm) and interquartile range (6.51 – 11.05 µm). Values from n = 4990 cells from 7 independent
639 experiments. (F) Distance of individual bacteria to the centroid of the host cell depending on its
640 bacterial load. Graph represents the median and interquartile range. Kruskal-Wallis test and
641 Dunn's multiple comparisons test. (G) Area of cells depending on infection. Graph represents
642 the median area (uninfected: 3031 μm^2, infected: 4148 μm^2) and interquartile range (unifected:
643 2308 – 4169 μm^2, infected: 3062 – 5752 μm^2). Values from n = 9469 uninfected cells and n =
644 1031 infected cells from 7 independent experiments. (H) Area of infected cells depending on its
645 bacterial load. Graph represents the median and interquartile range. Kruskal-Wallis test and
646 Dunn's multiple comparisons test. (I) Nuclear area of cells depending on infection. Graph
647 represents the median area (uninfected: 1551 μm^2, infected: 1897 μm^2) and interquartile range
648 (unifected: 1209 - 1950 μm^2, infected: 1486 - 2333 μm^2). Values from n = 9469 uninfected cells
649 and n = 1031 infected cells from 7 independent experiments. (J) Nuclear area of infected cells
650 depending on its bacterial load. Graph represents the median and interquartile range. Kruskal-
651 Wallis test and Dunn's multiple comparisons test.

652

653 **Figure 2: *S. flexneri* infection reduces host DNA synthesis and host protein synthesis.** (A)
654 Representative microscopy image of HeLa cells infected with *S. flexneri* expressing mCherry at
655 3 h.p.i, after 1h incubation with Click-IT Edu. Asterisks label the nucleus of infected cells with
656 reduced Edu incorporation. Contour of selected cells is delimited with a dashed line. Scale bar,
657 10 µm. (B) Edu acquisition in uninfected cells is bimodal. Graph represents the normalised
658 median of the ratio between the fluorescence intensity of Edu and Hoechst (1), and interquartile
659 range (0.5924 – 31.22). Values from n = 8941 cells from 3 independent experiments. An arbitrary
660 threshold of 5 is selected to define cells in S-phase. (C) Frequency of cells in S-phase (as defined
661 in B) depending on infection. Graph represents mean ± SD (uninfected: 34.45% ± 9.78%,
662 infected: 35.89% ± 4.69%). Student's t-test. (D) Edu acquisition in cells in S-phase depending
663 on infection. Graph representes the normalised median of the ratio between the fluorescence
664 intensity of Edu and Hoechst (uninfected: 75.14, infected: 44.73), and interquartile range
665 (uninfected: 27.89 – 131.0, infected: 22.05 – 93.36), from 3065 uninfected and 552 infected cells.
666 Mann-Whitney U test. (E) Edu acquisition in cells in S-phase depending on bacterial load. Graph
667 represents the median and interquartile range. Kruskal-Wallis test and Dunn's multiple
668 comparisons test. (F) Representative microscopy image of HeLa cells infected with *S. flexneri*
669 expressing mCherry at 3 h.p.i, after 1h incubation with Click-IT AHA. Asterisks label the
670 infected cells with reduced AHA incorporation. Scale bar, 10 µm. (G). AHA acquisition in host
671 cells depending on infection. Graph representes the normalised median of AHA fluorescence
672 intensity (uninfected: 1, infected: 0.86), and interquartile range (uninfected: 0.7850 – 2.694,
673 infected: 0.6207 – 1.241), from 36 uninfected and 233 infected cells. Mann-Whitney U test. (H)
674 AHA acquisition in infected cells depending on bacterial load. Graph represents the median and
675 interquartile range. Kruskal-Wallis test and Dunn's multiple comparisons test.
676

677 **Figure 3. Microscopy pipeline to automatically identify SEPT7-*S. flexneri* interactions.** (A)
678 Diagram representing the steps involved in the imaging and analysis pipeline. After infection,
679 fixation and staining, high number of images are automatically acquired using the high-content
680 microscope. Scale bar, 10 µm. These are then processed to segment bacteria based on their
681 fluorescence, so that a square field containing the bacteria in the centre is cropped and saved for
682 subsequent analysis. A deep learning model based on CNN is applied using Jupiter notebooks
683 and the Python Keras library hosted on Colab to sort individual, isolated bacteria. Several
684 processing steps are applied using Python to remove noise (band-pass filtering by difference of
685 Gaussian and mean filters), normalise the data across datasets for comparison, and remove signal
686 away from the bacteria which is irrelevant for the identification of SEPT7 assemblies. Scale bar,
687 1 µm. Finally, a similar second deep learning model based on CNN is applied to identify SEPT7
688 interacting with bacteria.
689
690 **Figure 4. Training of a deep learning algorithm to identify single isolated bacteria cells and**
691 **SEPT7 associated *S. flexneri*.** (A) Table summarizing the annotated dataset used for the training
692 process. The labels of the two classification classes used were "Single bacteria" and "Clump".
693 The annotated images were randomly split into two groups, one used as training dataset
694 (comprising 80% of the images) and another used as validation dataset (with the remaining 20%).
695 A separate annotated dataset was used for testing. (B) Representative Airyscan images of bacteria
696 used for each class. Scale bar, 1 µm. (C) Architecture of the deep learning algorithm used for
697 training. Each raw describes the characteristics of the sequential transformation steps applied.
698 Conv2D stands for 2D Convolution. (D, E) Accuracy and Loss as metrics to represent the training
699 process over subsequent epochs (entire passing of the training data through the algorithm).
700 Accuracy increases and loss decreases for both training and validation datasets, indicating a good
701 fit of the model to the data. Vertical dashed grey line indicates Early Stopping, or epoch value

for the minimum validation Loss. (F) Confusion matrix performed on an annotated test dataset not used previously for the training or validation process, indicating the percentage of predictions that were correct or wrong for each class. (G) Precision, recall and f1 score as metrics that summarize the performance of the model or classifier. (H) Table summarizing the annotated dataset used for the training process. The labels of the two classification classes used were "Septin" and "Negative". The annotated images were randomly split into three groups, one used as training dataset (comprising 75% of the images), another used as validation dataset (with 15%) and a last one used as test dataset (with 10%). Due to the data being very imbalanced (15% natural frequency of SEPT7 associated bacteria), the images comprised in the Negative class were under-sampled as indicated in the table. (I) Representative Airyscan images of bacteria used for each class. Scale bar, 1 µm. (J) Architecture of the deep learning algorithm used for training. Each raw describes the characteristics of the sequential transformation steps applied. Conv2D stands for 2D Convolution, Batch_norm stands for Batch normalisation. (K, L) Accuracy and Loss as metrics to represent the training process over subsequent epochs. Accuracy increases and loss decreases for both training and validation datasets, indicating a good fit of the model to the data. Vertical dashed grey line indicates Early Stopping, or epoch value for the minimum validation Loss. (M) Confusion matrix performed on the test dataset not used previously for the training or validation process, indicating the percentage of predictions that were correct or wrong for each class. (N) Precision, recall and f1 score as metrics that summarize the performance of the model or classifier.

Figure 5. Septin assemblies associated to *S. flexneri* are heterogeneous. (A) Selected examples of the training dataset to showcase the diverse morphology of septin assemblies associated to bacteria. Frequent morphologies include (a) ring like structures around the bacteria, (b) smooth tight recruitment around the entire bacterial surface, (c) loose structures more distant

727 from the bacterial surface, (d) septin recruitment to both bacterial poles, (e) septin recruitment to
728 a single bacterial pole. Scale bar, 1 µm. (B) Intensity profiles of the cytosolic bacterial mCherry
729 and the SEPT7 recruitment, as indicated in the white and orange dashed lines, respectively. (C)
730 Pie chart representing the relative frequency of 855 *S. flexneri*- SEPT7 associations depicted in
731 A.
732
733 **Figure 6. *S. flexneri* associated with SEPT7 are metabolically active.** (A) Representative
734 microscopy image of HeLa cells infected with *S. flexneri* expressing mCherry at 3 h.p.i, after 1h
735 incubation with Click-IT Edu. Scale bar 10 µm. (B) Enlarged view of insets in A, highlighting a
736 *S. flexneri* associated or not to SEPT7 structures. Scale bar, 1 µm. (C) Frequency of the number
737 of SEPT7-associated bacteria identified using deep learning from experiments in A, from n=
738 1024 from 3 independent replicates. Graph represents mean ± SD (9.23% ± 2.62%). (D)
739 Normalised ratio between Edu signal and mCherry in individual bacteria. Graph representes the
740 median (negatives: 1, septin associated: 1.059), and interquartile range (negatives: 0.8185 –
741 1.207, septin associated: 0.8573 – 1.487). Mann-Whitney U test. (E) Representative microscopy
742 image of HeLa cells infected with *S. flexneri* expressing mCherry at 3 h.p.i, after 1h incubation
743 with Click-IT AHA. Scale bar 10 µm. (F) Enlarged view of insets in E, highlighting a *S. flexneri*
744 associated or not to SEPT7 assemblies. Scale bar, 1 µm. (G) Frequency of the number of SEPT7-
745 associated bacteria identified using deep learning from experiments in E, from n = 1872 bacteria
746 from 3 independent replicates. Graph represents mean ± SD (7.01% ± 2.41%). (D) Normalised
747 AHA signal in individual bacteria in A, B. Graph representes the median (negatives: 1, SEPT7
748 associated: 1.055), and interquartile range (negatives: 0.6986 – 1.345, SEPT7 associated: 0.7837
749 – 1.497). Mann-Whitney U test.
750

751 **Figure 7. *S. flexneri* associated with SEPT7 have an active T3SS.** (A) Representative
752 microscopy image of HeLa cells infected with *S. flexneri* expressing the TSAR reporter at 3 h.p.i.
753 Scale bar 10 µm. Arroheads highlight TSAR+ bacteria. Selected infected cells contours are
754 delimited with dashed lines. (B) Distribution of TSAR signal intensity in individual bacteria.
755 Graph represents the normalised median of the ratio between TSAR and mCherry (1), and
756 interquartile range (0.7827 – 1.369). Values from n = 3654 bacterial cells from 3 independent
757 experiments. An arbitrary threshold of 1.5 is selected to define TSAR+ *S. flexneri*. (C) Intensity
758 of TSAR signal in individual bacteria depending on infection load of host cells. Graph represents
759 the normalised median and interquartile range. Kruskal-Wallis test and Dunn's multiple
760 comparisons test. (D) Representative microscopy image of HeLa cells infected with *S. flexneri*
761 expressing the TSAR reporter at 3 h.p.i. Scale bar 10 µm. (E) Enlarged view of insets in D,
762 highlighting a *S. flexneri* associated or not to SEPT7 assemblies. Scale bar, 1 µm. (F) Frequency
763 of the number of SEPT7-associated bacteria identified using deep learning from experiments in
764 F, from n= 5030 bacteria from 4 independent replicates. Graph represents mean ± SD (9.044% ±
765 5.582%). (G) Percentage of TSAR+ *S. flexneri* depending on their association to SEPT7. Graph
766 represents mean ± SD (negatives: 2.214 ± 1.603, septin associated: 17.74 ± 5.138). Student's t-
767 test. (H) Normalised ratio between TSAR signal and mCherry in individual bacteria. Graph
768 representes the median (negatives: 1, SEPT7 associated: 1.122), and interquartile range
769 (negatives: 0.7674 – 1.286, SEPT7 associated: 0.9047 – 1.511). Mann-Whitney U test.

770 **Supplementary Figure Legends.**

771 **Figure 1-figure supplement 1. *S. flexneri* infection induces host cell size changes.** (A)
772 Hoestch fluorescence intensity of sum-projected nuclei as proxy of nuclear volume. Graph
773 represents normalised median (uninfected: 1, infected: 1.294) and interquartile range (uninfected:
774 0.7588 – 1.287, infected: 0.9534 – 1.878) of n=2071 uninfected cells and n=195 infected cells
775 from 3 independent experiments. Mann-Whitney U test. (B – C) Cell and nuclear area in presence
776 and absence of infection and Latrunculin B. Graph represents the median and interquartile range.
777 Kruskal-Wallis test and Dunn's multiple comparisons test.

778

779 **Figure 2-figure supplement 1. Click-IT Edu and Click-IT AHA specifically label *de novo***
780 **DNA and protein synthesis in Hela cells.** (A) Representative widefield image of HeLa cells
781 after Click-IT Edu reaction in the presence or absence of Aphidicolin to inhibit eukaryotic DNA
782 replication. Scale bar, 10 µm. (B) Quantification of *de novo* DNA synthesis in single HeLa cells
783 in A as the ratio of nuclear Click-IT Edu signal to Hoechst. Graph represents the normalised
784 median (untreated: 1, Aphidicolin: 0.7667) and interquartile range (untreated: 0.8474 – 6.571,
785 Aphidicolin: 0.6816 – 0.8543) from 15828 untreated and 14943 treated cells from 3 independent
786 experiments. Mann-Whitney U test. (C) Representative Airyscan confocal images of HeLa cells
787 after Click-IT AHA reaction in the presence or absence of Cycloheximide to block eukaryotic
788 translational elongation. Scale bar, 10 µm. (D) Quantification of cytoplasmic Click-IT AHA
789 signal of the HeLa cells in A. Graph represents normalised median (untreated: 1, Cycloheximide:
790 0.3531) and interquartile range (untreated :0.6794 – 1.401, Cycloheximide: 0.2504 – 0.6637) of
791 n=268 untreated and n= 258 Cycloheximide treated cells from 3 independent experiments. Mann-
792 Whitney U test.

793

794 **Figure 4-figure supplement 1. Additional examples of the annotated datasets for deep**
795 **learning.** (A) Representative images of multiple bacteria associated to SEPT7. Scale bar, 1 µm.
796 (B) Representative images of the training and validation dataset to identify single bacteria versus
797 clumps. Scale bar, 5 µm. (C) Representative images of the training and validation dataset to
798 identify SEPT7-positive versus SEPT7-negative bacteria, after processing. Scale bar, 5 µm.
799
800 **Figure 5-figure supplement 1. Probability maps of SEPT7 around *S. flexneri.*** (A, C) Median
801 of the signal for mCherry and SEPT7 in both datasets (SEPT7-positive and SEPT7-negative),
802 centered at the bacterial midbody or bacterial pole, respectively. Only bacteria with width ≥ 2.5
803 µm were selected to ensure bacteria were mostly transversal to the acquisition axis. Scale bar, 1
804 µm. (B,C) Quantification of SEPT7 signal and *S. flexneri* mCherry signal in the midbody
805 projection depicted in A and transversal dash line indicated in B.
806
807 **Figure 6-figure supplement 1. Click-IT Edu and Click-IT AHA specifically label *de novo***
808 **DNA and protein translation in *S. flexneri.*** (A) Representative Airyscan image of mCherry *S.*
809 *flexneri* after Click-IT Edu reaction in the presence or absence of Nalidixic acid to block bacterial
810 DNA replication. Scale bar, 1 µm. (B) Quantification of Click-IT Edu signal of bacteria in C
811 measured by FACS. Graph represents normalised mean ± SD. One-way ANOVA and Tukey's
812 multiple comparisons test. (C) Representative Airyscan confocal images of HeLa cells infected
813 with mCherry expressing *S. flexneri* after Click-IT Edu reaction in the presence or absence of
814 Nalidixic acid to inhibit bacterial DNA nuclear replication. Scale bar, 10 µm. (D) Quantification
815 of *de novo* DNA synthesis in single bacteria in E as the ratio of nuclear Click-IT signal to
816 Hoechst. Graph represents normalised median (untreated: 1, Nalidixic acid: 0.0646) and
817 interquartile range (untreated: 0.3589 – 1.924, Nalidixic acid: 0.0350 – 0.3080) of 9310 untreated
818 and 4368 Nalidixic acid treated bacteria from 3 independent experiments. Mann-Whitney U test.

819 (E) Representative Airyscan confocal images of HeLa cells infected with mCherry expressing *S.*
820 *flexneri* after Click-IT AHA reaction in the presence or absence of Rifampicin to block
821 prokaryotic translation. Scale bar, 10 µm; insets, 1 µm. (F) Quantification of cytoplasmic Click-
822 IT AHA signal of individual *S. flexneri* cells in C. Graph represents normalised median
823 (untreated: 1, Rifampicin: 0.8263) and interquartile range (untreated: 0.7520 – 1.350,
824 Rifampicin: 0.6143 – 1.100) of n=2309 untreated and n=345 Rifampicin treated bacteria from 3
825 independent experiments.
826
827 **Figure 7-figure supplement 1. TSAR labels T3SS activity specifically.** (A) Representative
828 Airyscan confocal images of *S. flexneri* harbouring the TSAR plasmid grown in broth in the
829 presence or absence of congo red to induce the expression of the T3SS. Scale bar, 1 µm. (B)
830 Quantification of the TSAR dependent GFP signal of bacteria in A measured by FACS. Graph
831 represents the normalised mean ± SD (untreated: 1 ± 0, congo red: 155.4 ± 125.2) from 4
832 independent experiments. (C) Representative examples of TSAR-positive *S. flexneri* associated
833 to SEPT7. C stands for "cage", P stands for "protrusion". Scale bar 5 µm.

Figure 1

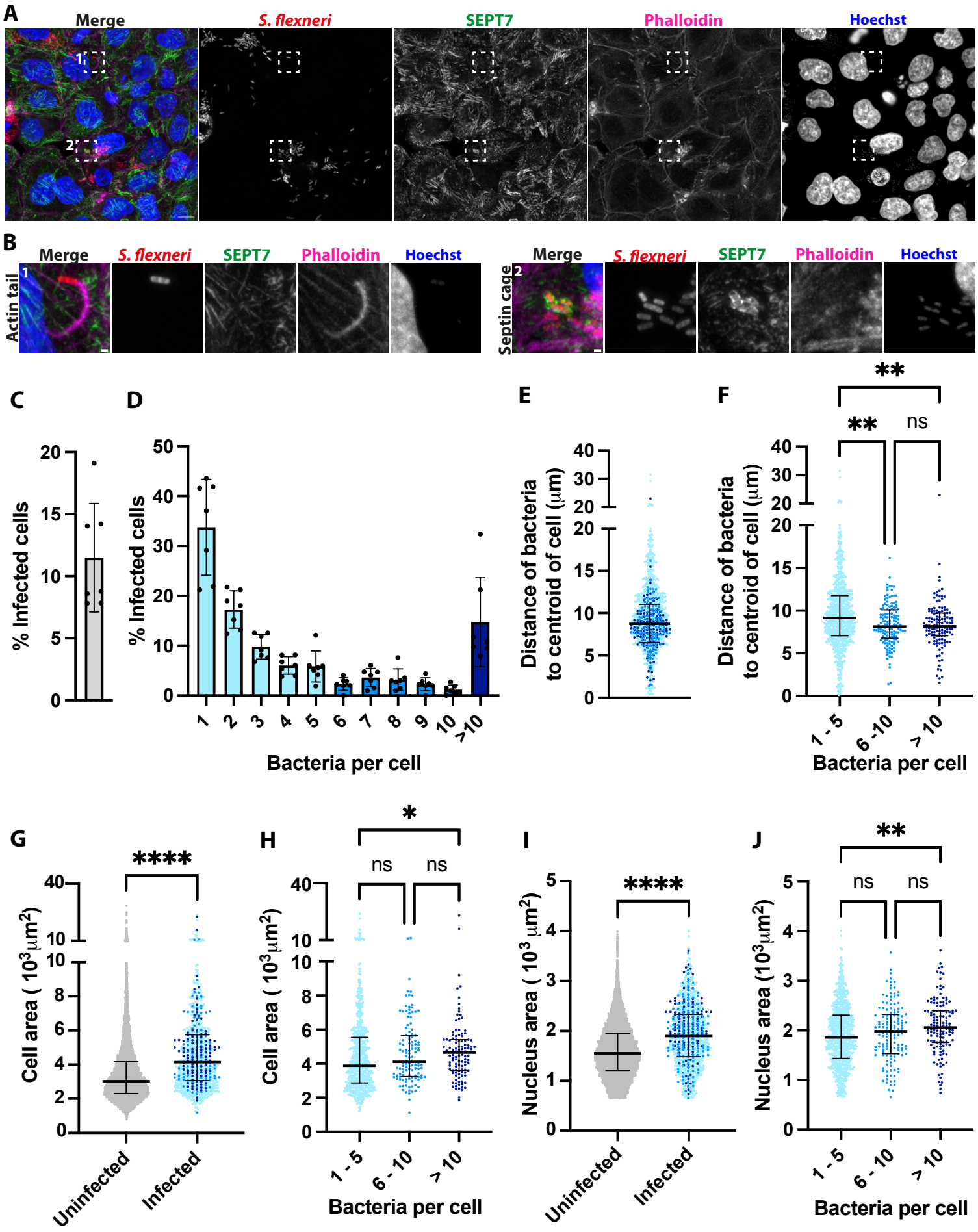
A
Merge
S. flexneri
SEPT7
Phalloidin
Hoechst
1
2
B
Actin tail
Septin cage
C
% Infected cells
D
% Infected cells
Bacteria per cell
1 2 3 4 5 6 7 8 9 10 >10
E
Distance of bacteria to centroid of cell (µm)
F
Distance of bacteria to centroid of cell (µm)
**
ns
1 - 5
6 - 10
> 10
Bacteria per cell
G
****
Cell area (10³µm²)
Uninfected
Infected
H
*
ns
Cell area (10³µm²)
Bacteria per cell
I
****
Nucleus area (10³ µm²)
Uninfected
Infected
J
**
ns
Nucleus area (10³µm²)
Bacteria per cell

Figure 2

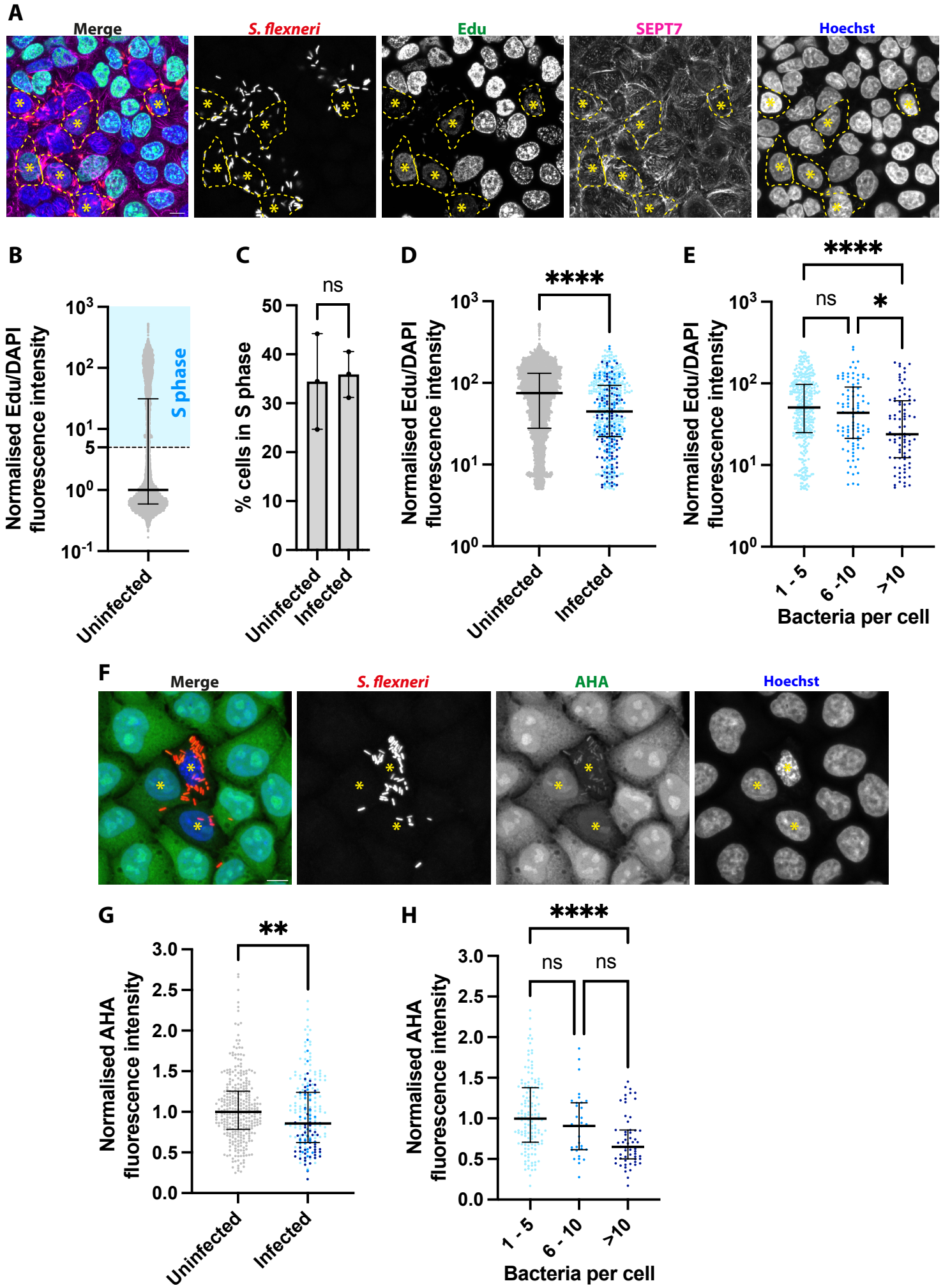
A
Merge
S. flexneri
Edu
SEPT7
Hoechst
B
Normalised Edu/DAPI fluorescence intensity
S phase
Uninfected
C
ns
% cells in S phase
Uninfected
Infected
D
****
Normalised Edu/DAPI fluorescence intensity
Uninfected
Infected
E
****
ns
*
Normalised Edu/DAPI fluorescence intensity
1 - 5
6 -10
>10
Bacteria per cell
F
Merge
S. flexneri
AHA
Hoechst
G
**
Normalised AHA fluorescence intensity
Uninfected
Infected
H
****
ns
ns
Normalised AHA fluorescence intensity
1 - 5
6 - 10
>10
Bacteria per cell

Figure 3

A

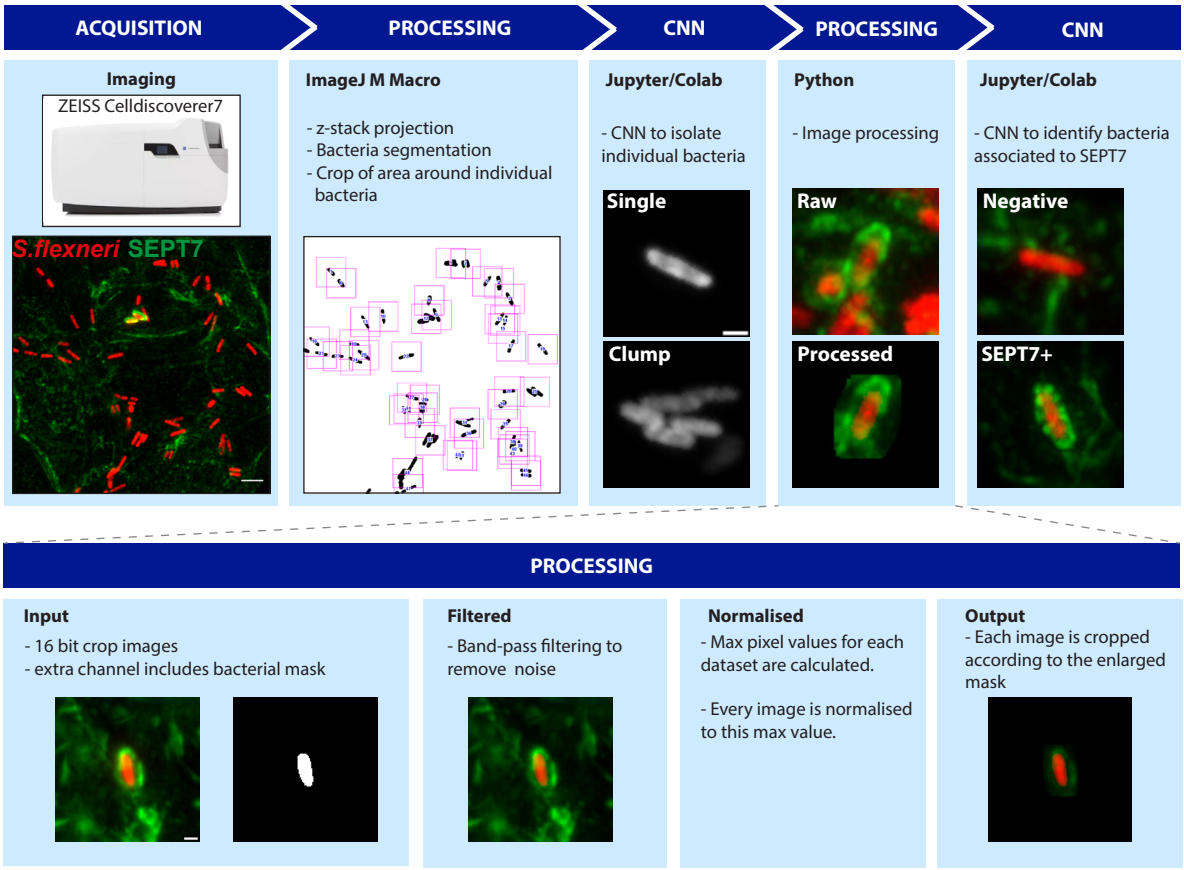
ACQUISITION
PROCESSING
CNN
PROCESSING
CNN
Imaging
ZEISS Celldiscoverer7
S.flexneri SEPT7
ImageJ M Macro
- z-stack projection
- Bacteria segmentation
- Crop of area around individual bacteria
Jupyter/Colab
- CNN to isolate individual bacteria
Single
Clump
Python
- Image processing
Raw
Processed
Jupyter/Colab
- CNN to identify bacteria associated to SEPT7
Negative
SEPT7+
PROCESSING
Input
- 16 bit crop images
- extra channel includes bacterial mask
Filtered
- Band-pass filtering to remove noise
Normalised
- Max pixel values for each dataset are calculated.
- Every image is normalised to this max value.
Output
- Each image is cropped according to the enlarged mask

Figure 4

A

Label	N° of images	Dataset 1	2	3	4
Single bact.	1209	885	0	143	181
Clump	933	253	578	35	67

Dataset 1 and 2: training 80%, validation 20%. Dataset 3 and 4: test.

B

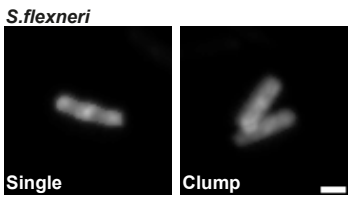

C

Model: "sequential" Total trainable parameters: 25,154

Layer	Output shape	Parameters
Conv2D (1)	(None, 126, 126, 4)	40
MaxPooling2D	(None, 63, 63, 4)	0
Conv2D (2)	(None, 61, 61, 8)	296
MaxPooling2D	(None, 30, 30, 8)	0
Conv2D (3)	(None, 28, 28, 16)	1,168
MaxPooling2D	(None, 14, 14, 16)	0
Conv2D (4)	(None, 12, 12, 32)	4,640
MaxPooling2D	(None, 6, 6, 32)	0
Conv2D (5)	(None, 4, 4, 64)	18,496
MaxPooling2D	(None, 2, 2, 64)	0
Flatten	(None, 256)	0
Dense	(None, 2)	514
Activation	(None, 2)	0

D

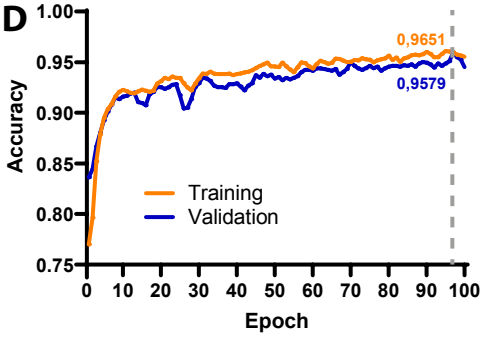

E

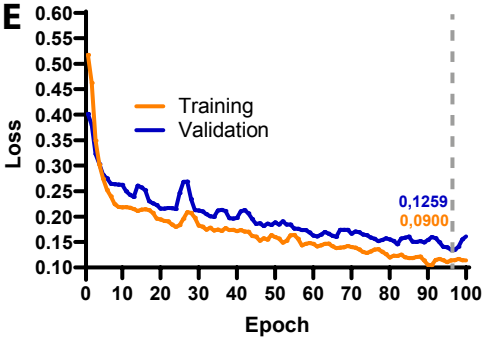

F

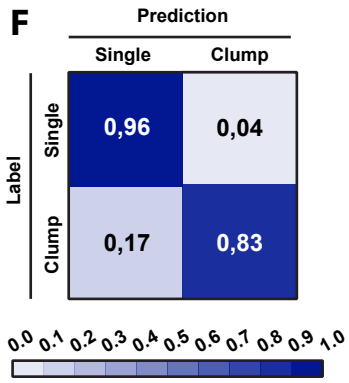

G

	Single	Clump
Precision	0.95	0.90
Recall	0.96	0.83
f1 score	0.95	0.86

H

Label	Total images	Dataset 1	2	3	4	5	6
SEPT7+	1203	43	802	68	47	141	102
Negatives	1498	203	758	29	10	498	0

Training 75%, validation 15%, test: 10%.

I

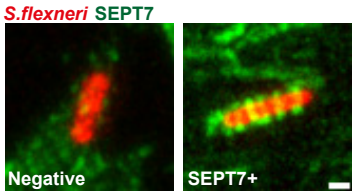

J

Model: "sequential" Total trainable parameters: 56,329

Layer	Output shape	Parameters
Conv2D (1)	(None, 126, 126, 4)	112
Batch_norm (1)	(None, 126, 126, 4)	16
MaxPooling2D (1)	(None, 63, 63, 4)	0
Conv2D (2)	(None, 61, 61, 8)	296
Batch_norm (2)	(None, 61, 61, 8)	32
MaxPooling2D (2)	(None, 30, 30, 8)	0
Conv2D (3)	(None, 28, 28, 16)	1,168
Conv2D (4)	(None, 26, 26, 16)	2,320
Batch_norm (3)	(None, 26, 26, 16)	64
MaxPooling2D (3)	(None, 13, 13, 16)	0
Conv2D (5)	(None, 11, 11, 32)	4,640
Conv2D (6)	(None, 9, 9, 32)	9,248
Batch_norm (4)	(None, 9, 9, 32)	128
MaxPooling2D (4)	(None, 4, 4, 32)	0
Conv2D (7)	(None, 2, 2, 64)	18,496
Batch_norm (5)	(None, 2, 2, 64)	256
MaxPooling2D (5)	(None, 1, 1, 64)	0
Flatten	(None, 64)	0
Dense (1)	(None, 300)	19,500
Activation (1)	(None, 300)	0
Dense (2)	(None, 1)	301
Activation (2)	(None, 3)	0

K

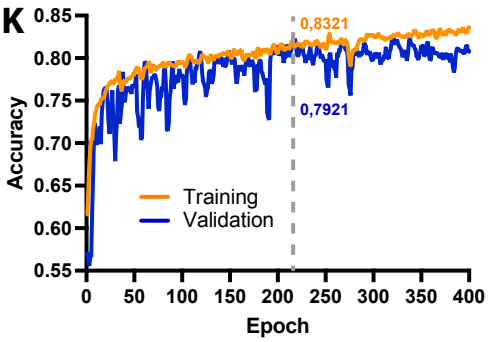

L

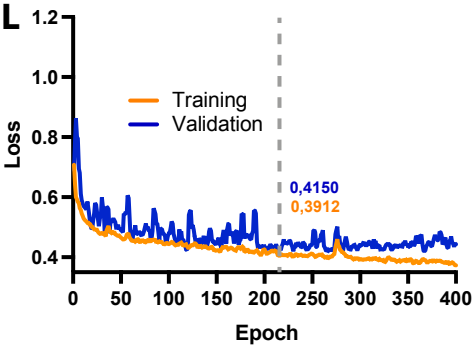

M

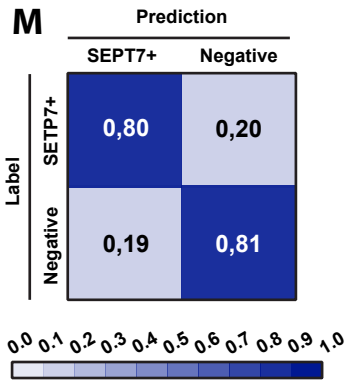

N

	SEPT7+	Negative
Precision	0.78	0.84
Recall	0.80	0.81
f1 score	0.79	0.83

Figure 5

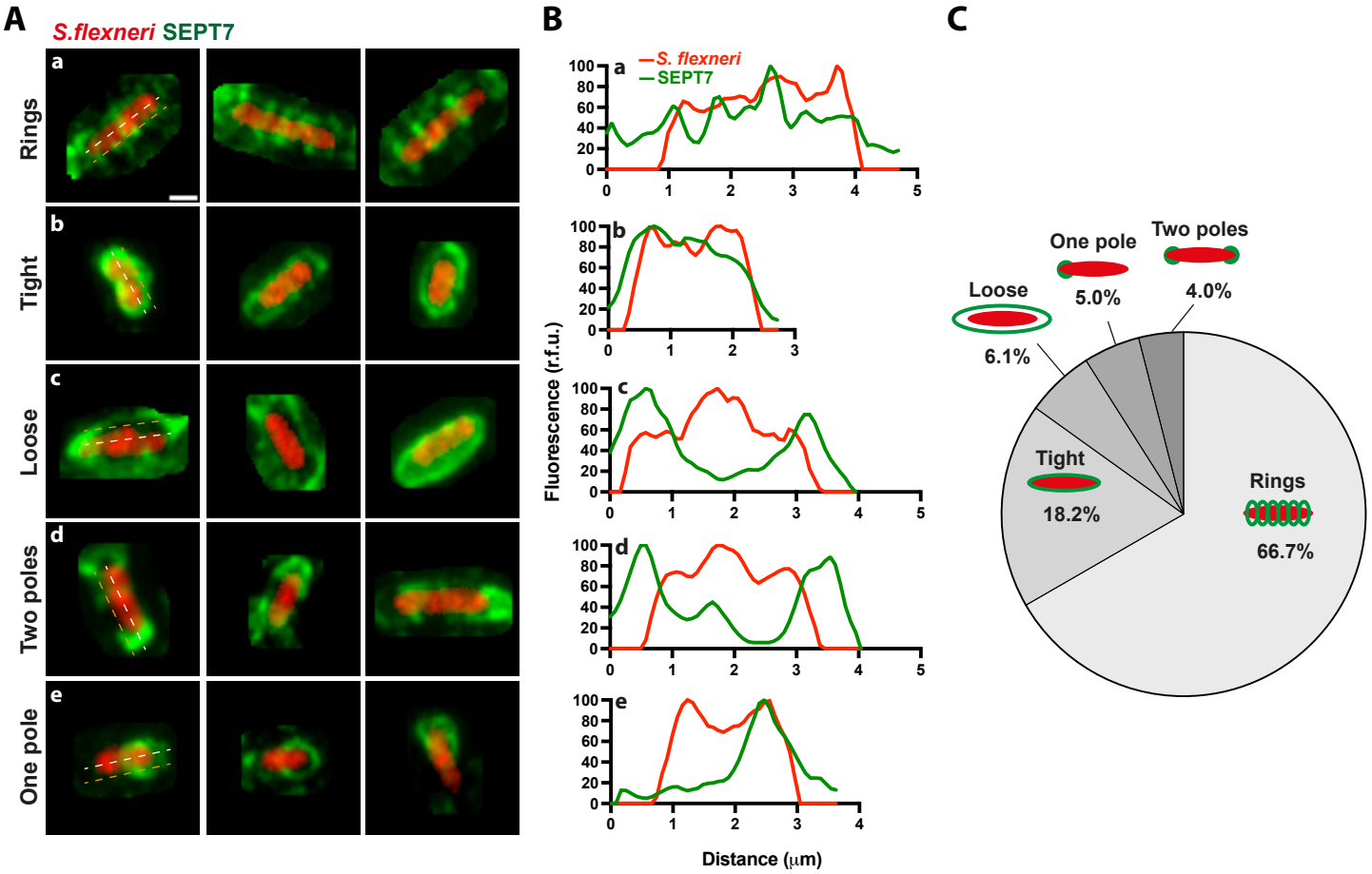
A
S.flexneri SEPT7
Rings
Tight
Loose
Two poles
One pole
a
b
c
d
e
B
S. flexneri
SEPT7
Fluorescence (r.f.u.)
Distance (μm)
C
Loose
6.1%
One pole
5.0%
Two poles
4.0%
Tight
18.2%
Rings
66.7%

Figure 6

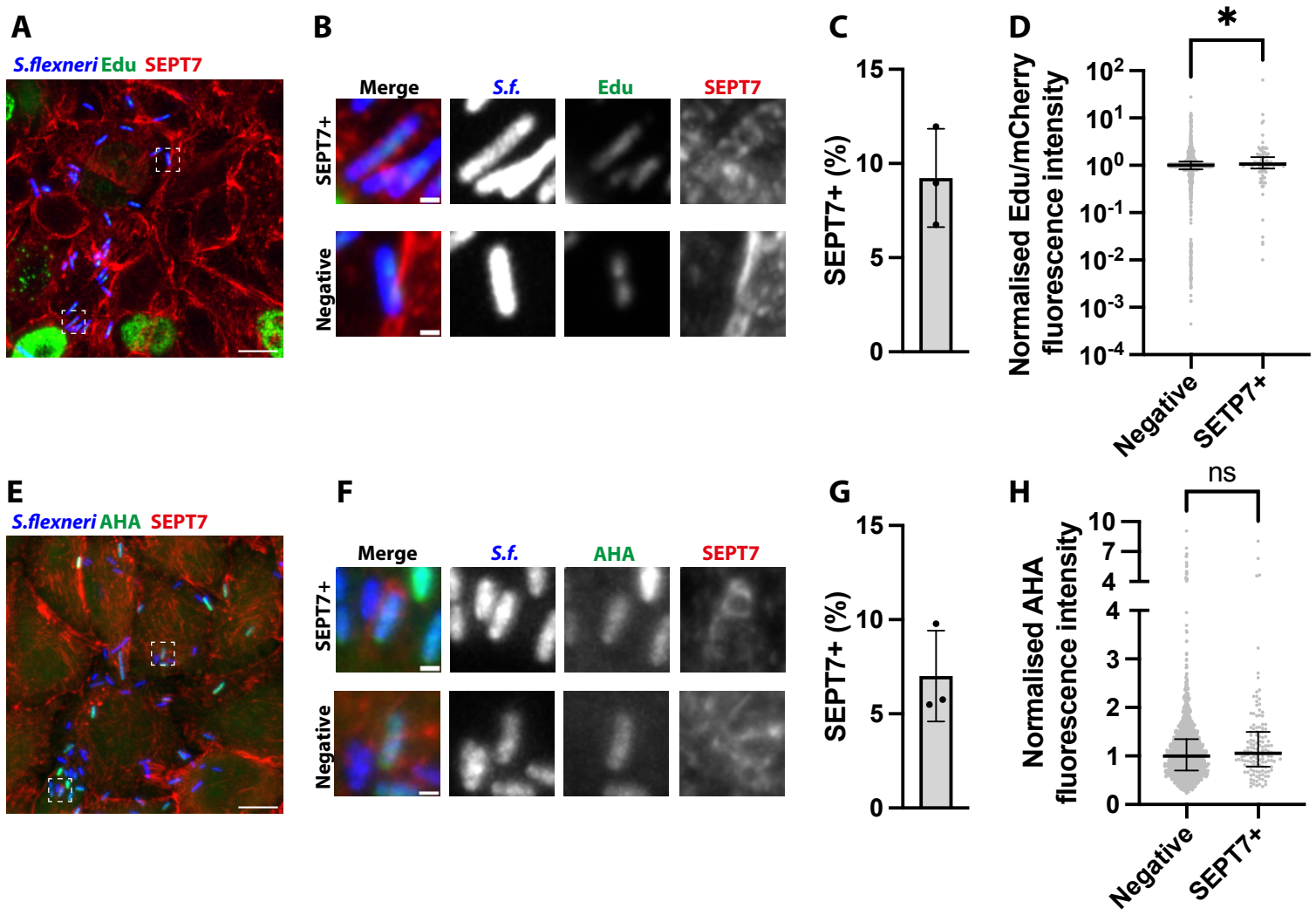
A
S.flexneri Edu SEPT7
B
Merge
S.f.
Edu
SEPT7
SEPT7+
Negative
C
SEPT7+ (%)
15
10
5
0
D
*
Normalised Edu/mCherry fluorescence intensity
10^2
10^1
10^0
10^{-1}
10^{-2}
10^{-3}
10^{-4}
Negative
SETP7+
E
S.flexneri AHA SEPT7
F
Merge
S.f.
AHA
SEPT7
SEPT7+
Negative
G
SEPT7+ (%)
15
10
5
0
H
ns
Normalised AHA fluorescence intensity
10
7
4
4
3
2
1
0
Negative
SEPT7+

Figure 7

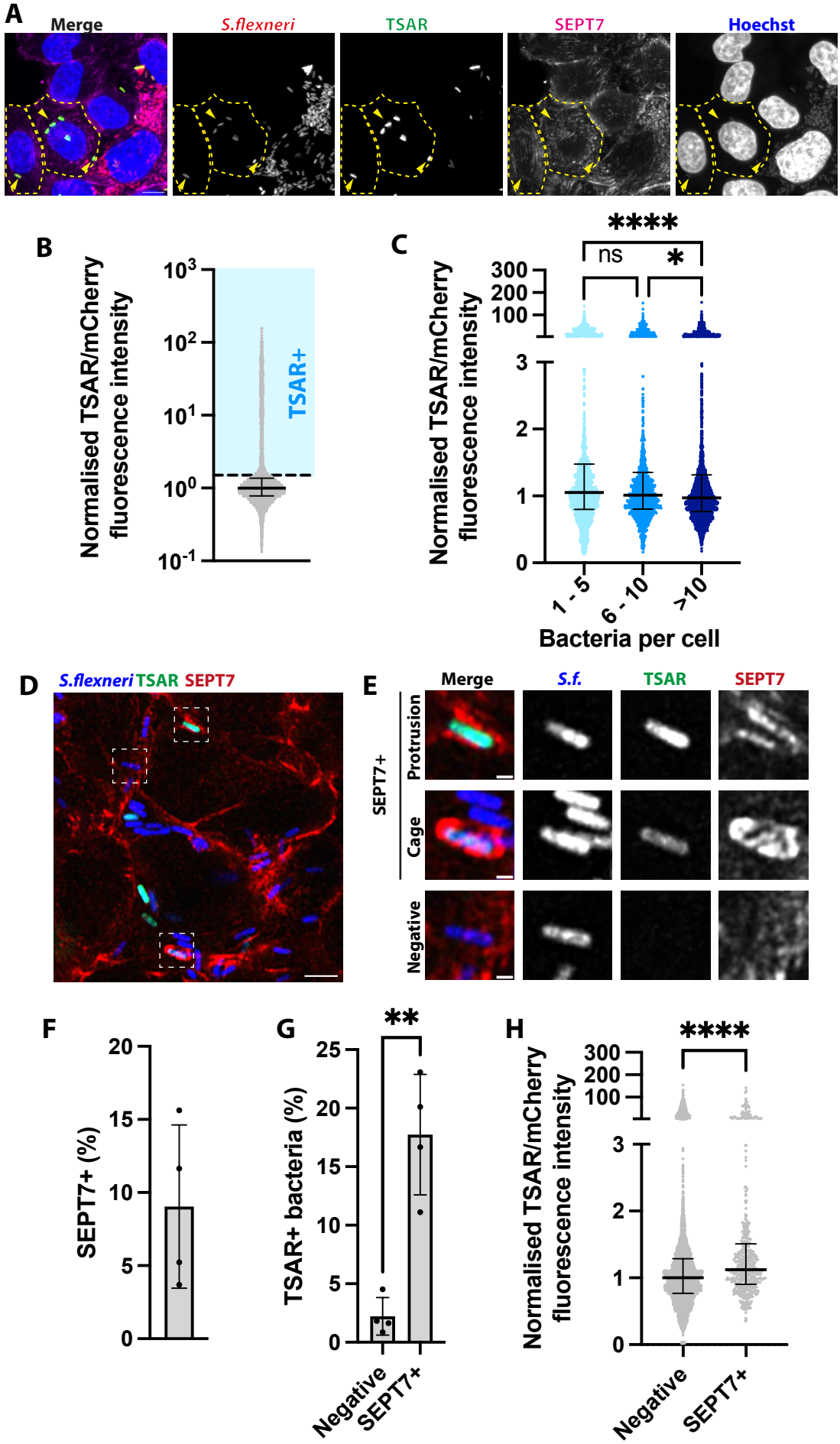
A
Merge
S.flexneri
TSAR
SEPT7
Hoechst
B
Normalised TSAR/mCherry fluorescence intensity
TSAR+
C
****
ns
*
Normalised TSAR/mCherry fluorescence intensity
1 - 5
6 - 10
>10
Bacteria per cell
D
S.flexneri TSAR SEPT7
E
Merge
S.f.
TSAR
SEPT7
SEPT7+
Protrusion
Cage
Negative
F
SEPT7+ (%)
G
**
TSAR+ bacteria (%)
Negative
SEPT7+
H
****
Normalised TSAR/mCherry fluorescence intensity
Negative
SEPT7+

Figure 1-figure supplement 1

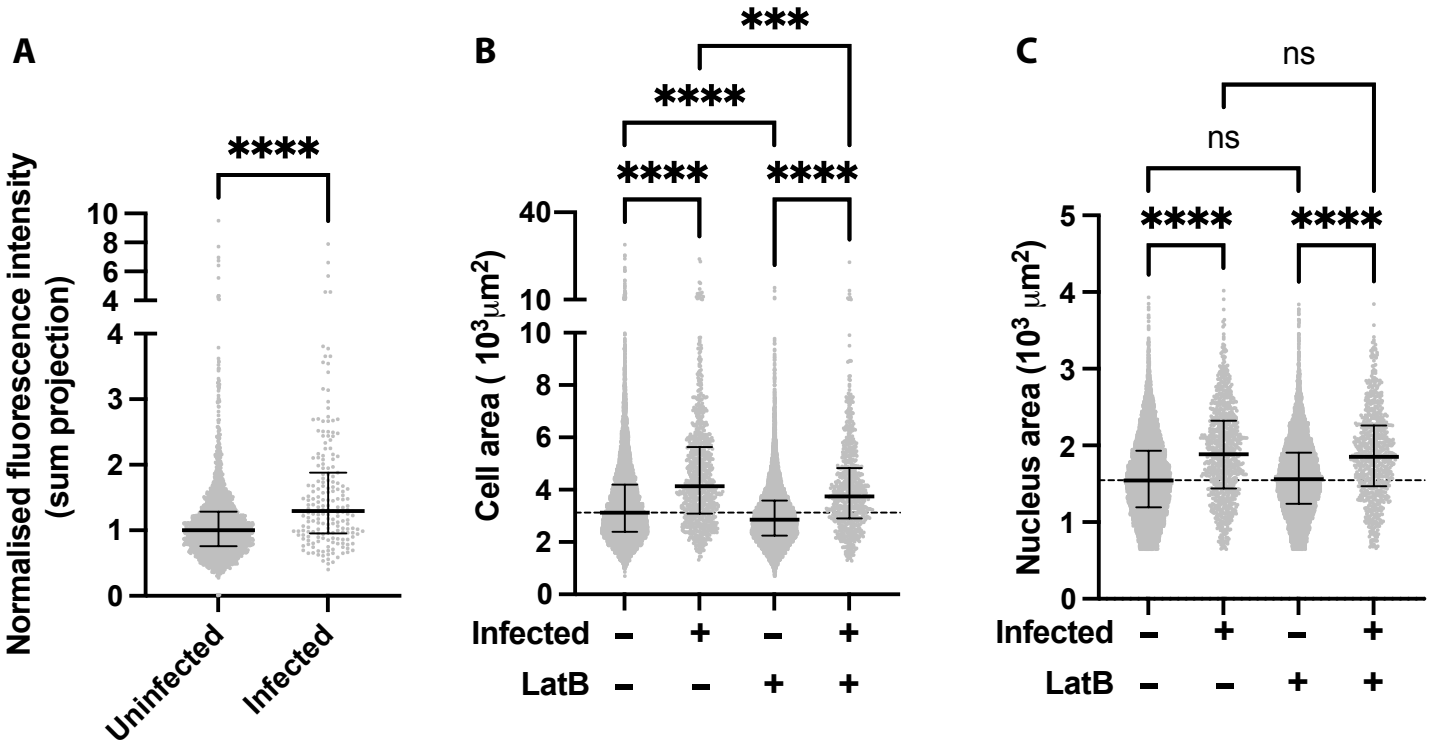

Figure 2-figure supplement 1

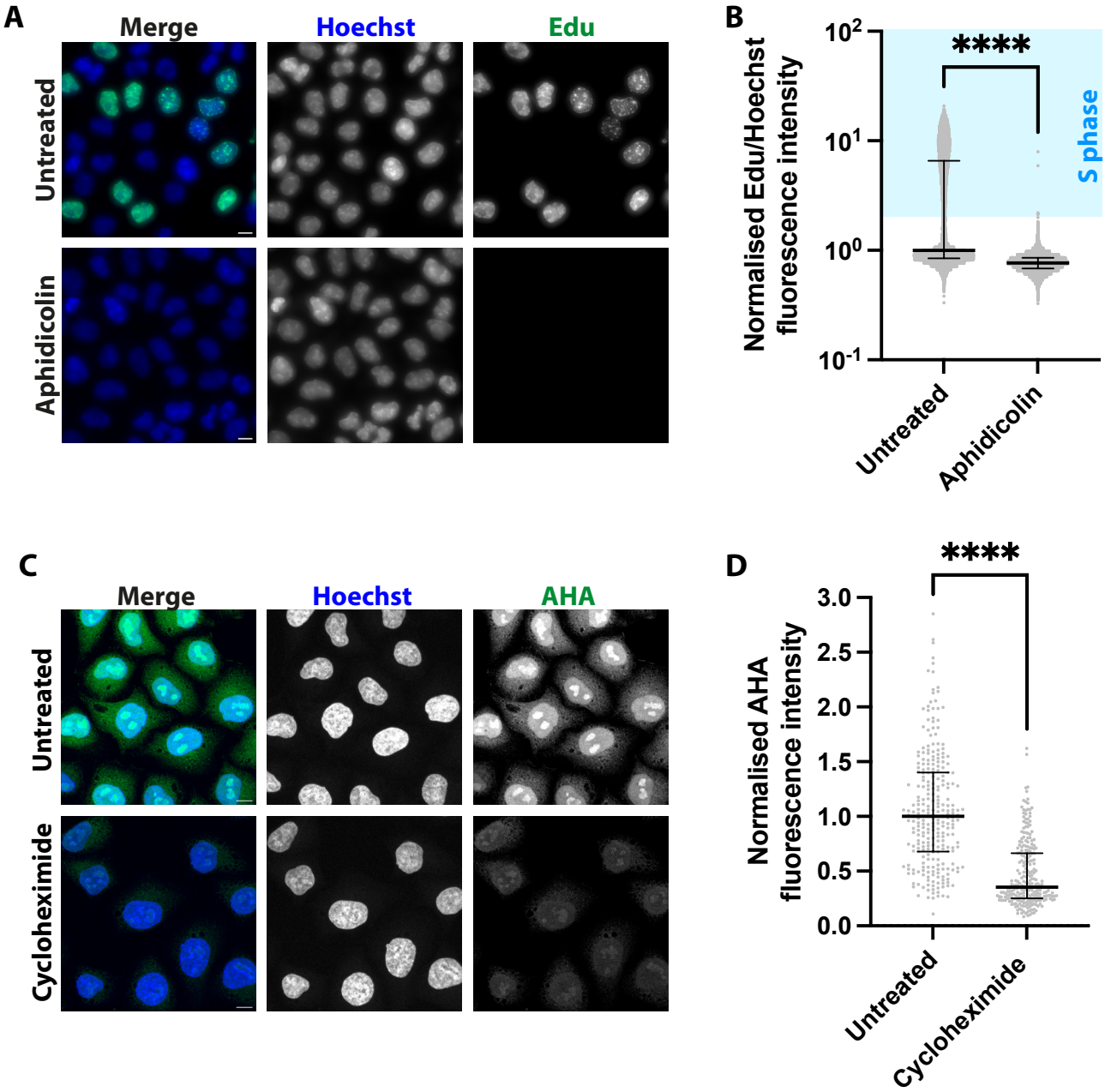

Figure 4-figure suplement 1

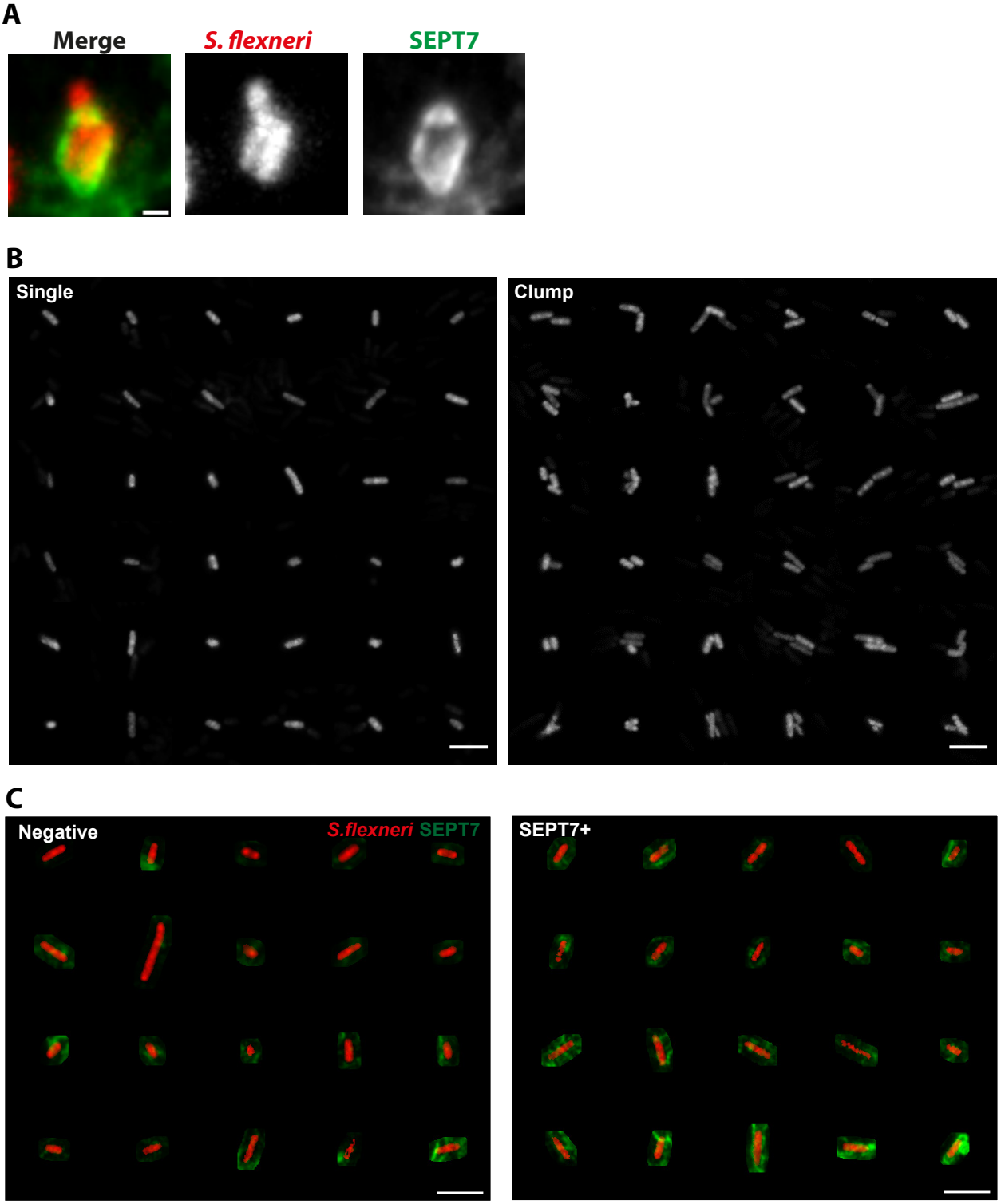

Figure 5-figure supplement 1

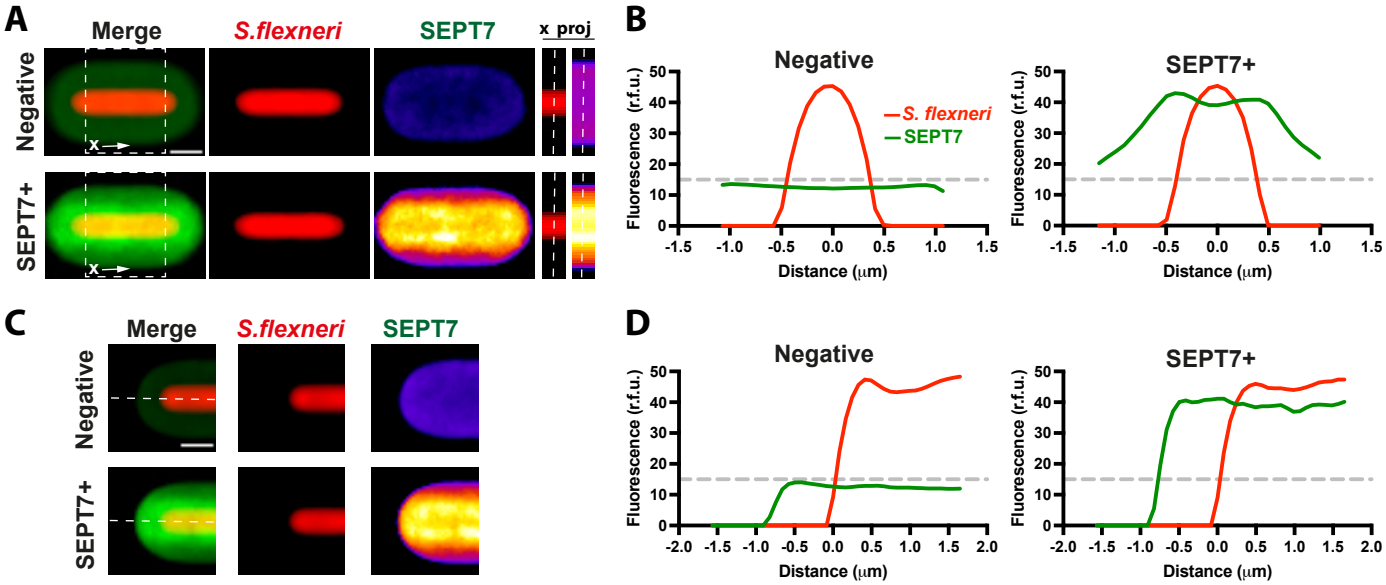

Figure 6-figure supplement 1

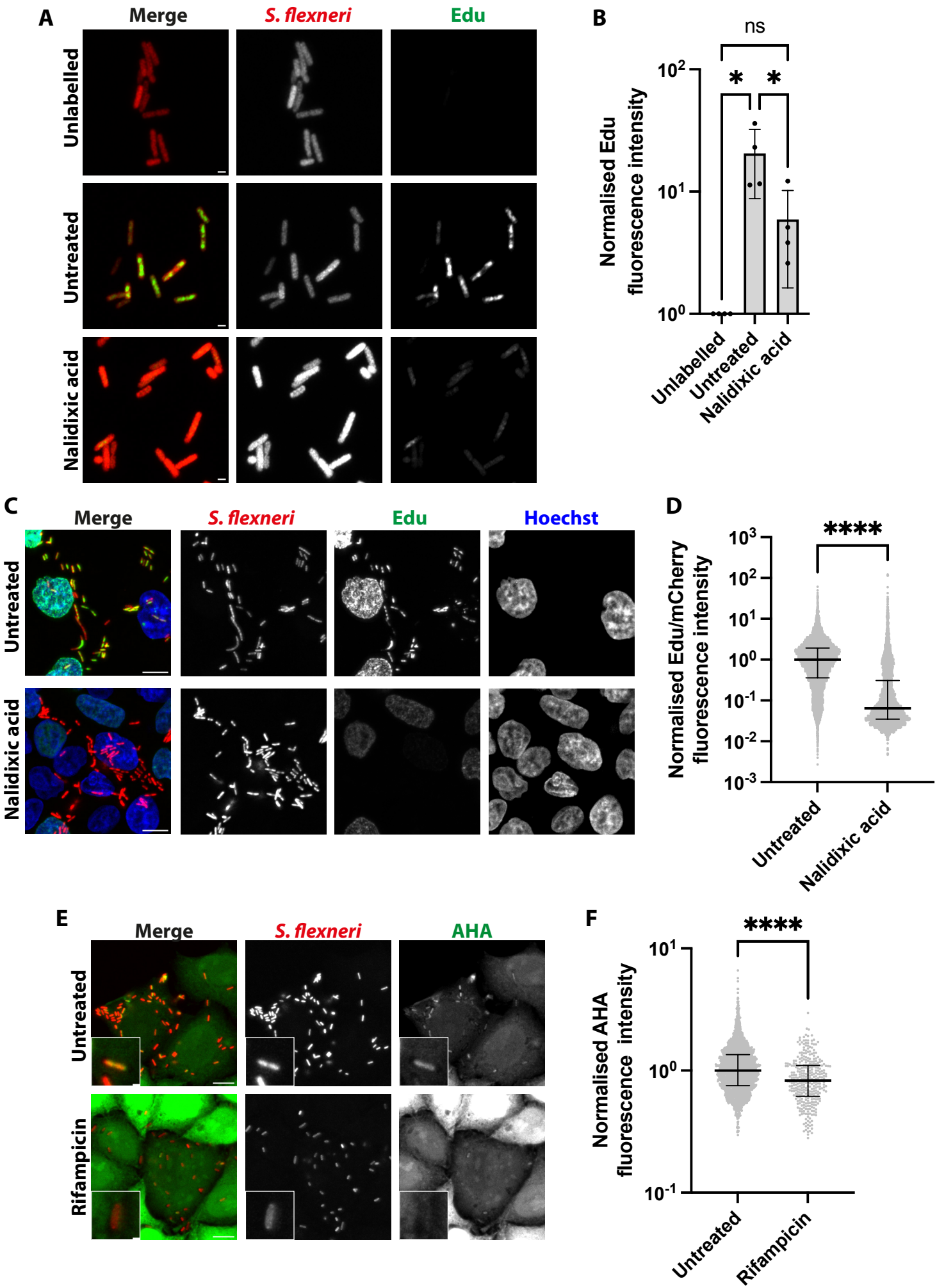
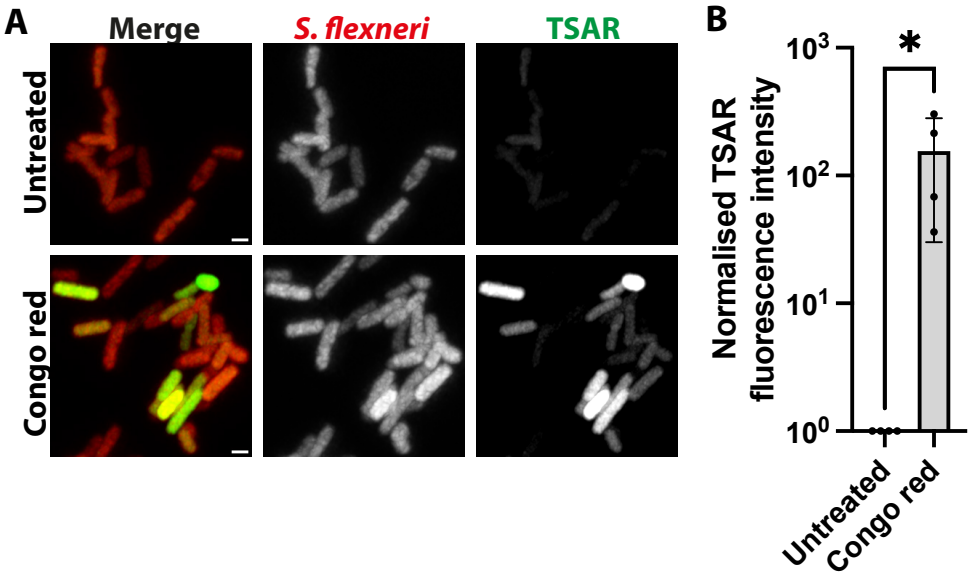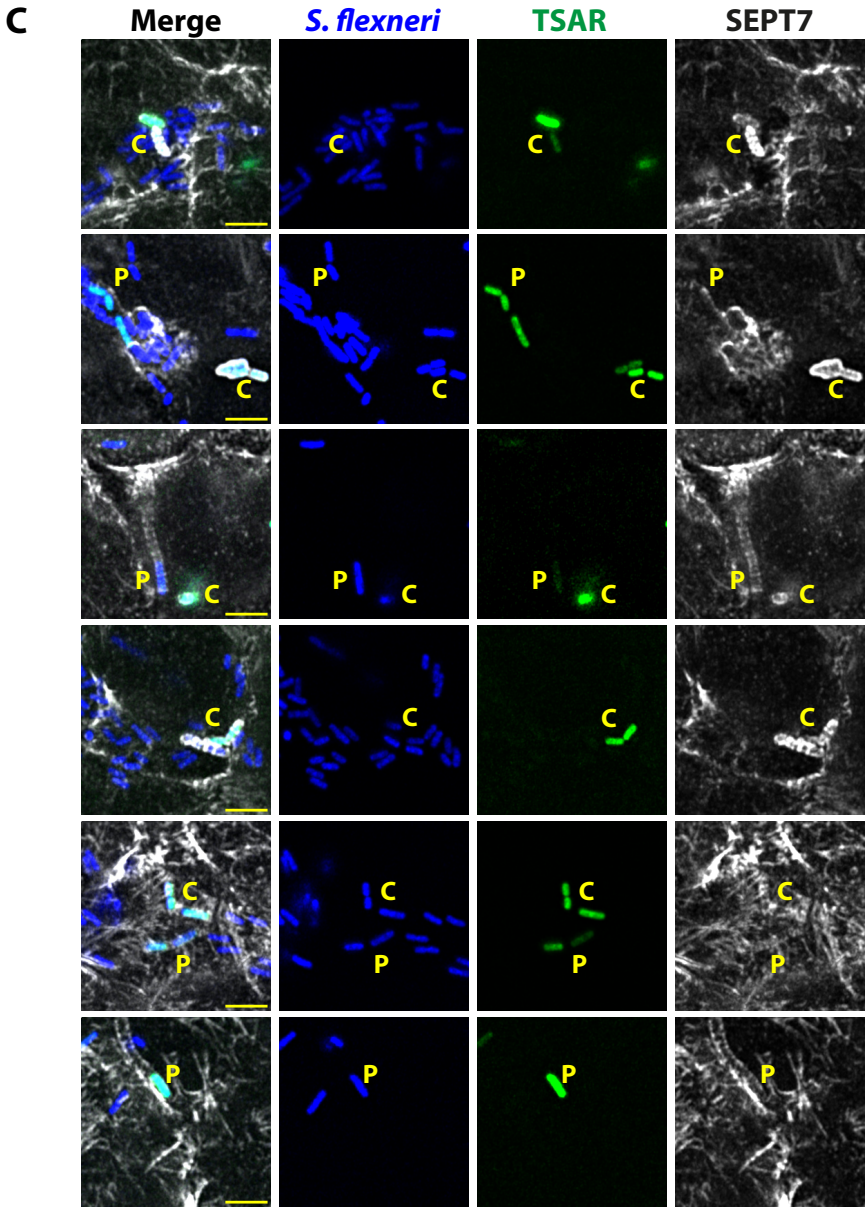
Figure 7-figure supplement 1